Catarina Sofia Jóia de Oliveira dos Santos

Licenciada em Ciências da Engenharia do Ambiente

Shoreline response to a sandy nourishment in a wave-dominated coast using video monitoring

Dissertação para a obtenção do Grau de Mestre em Engenharia do Ambiente, Perfil de Engenharia de Sistemas Ambientais

Orientador:

Professor Doutor José Carlos Ribeiro Ferreira, Professor Auxiliar na Faculdade de Ciências e Tecnologia da Universidade Nova de Lisboa

Coorientador:

Doutor Umberto Andriolo, Investigador Pós-Doutorado no Instituto de Engenharia de Sistemas e Computadores de Coimbra da Universidade de Coimbra

Júri:

Presidente: Professora Doutora Maria Júlia Fonseca Seixas

Arguente: Doutora Ana Maria Nobre Silva

Vogal: Professor Doutor José Carlos Ribeiro Ferreira

Junho, 2020

FACULDADE DE CIÊNCIAS E TECNOLOGIA
UNIVERSIDADE NOVA DE LISBOA

[Página deixada intencionalmente em branco.]

Shoreline response to a sandy nourishment in a wave-dominated coast using video monitoring

[Página deixada intencionalmente em branco.]

Acknowledgements

While the dissertation is an individual document, I would not have been able to finish it without the support of many people who inspired and encouraged me throughout the entire process.

I want to thank my thesis advisor, Professor Doutor José Carlos, for trusting me – and for all the guidance, support, and dedication during the development of this dissertation. To my co-advisor, Doutor Umberto Andriolo, a big thank you, for all the help, availability, and patience to guide me through the video monitoring basics and writing of a scientific article.

To my parents, who have always loved and supported me. Thank you for standing by me through all my bad decisions (choosing the wrong major at first, choosing the wrong country to study abroad) and for always believing I am a smart, strong, independent woman – even when I did not. To my brother, Sérgio, and to my cousins, Rui, Lili and Francisca. I love you all.

To my beautiful friends from my hometown, for always being there for me. To Flávia, for turning me into a very organized person whenever she decided to surprise visit Portugal while living in Qatar, so I could always hang out with her. To Maria and Martão, for being my most beautiful, smartest friends, who always make me laugh and have a nice word to say. To Mariana, for being present since we were 10 – despite having lived in ten thousand different cities and countries ever since.

To my uni friends. To Ana, for being my friend since the first week at university – for always supporting me, for always wanting to party, and for being the most annoying person I know. To Clara, for always being there for me, for being my gym and shopping company, and for being my SMA. To Diogo, for buying me lunch on the first day we met, for being my friend ever since, and for being my most relatable friend ever. To Maria, the strongest and most brilliant friend I have! And to Ana Seco, my "mom", who always has nice, kind, and reassuring words to say. I love you!

And, last but certainly not least, to my colleagues from 103. Filipa, Joana, Renato, and Cláudio, thank you for adopting me and for being the greatest colleagues/friends anyone could ask for.

[Página deixada intencionalmente em branco.]

Abstract

Beach nourishment is a soft engineering intervention that supplies sand to the shore, to increase the beach recreational area and to decrease coastal vulnerability to erosion. This study presents the preliminary evaluation of nourishment works performed at the high-energy wave-dominated Portuguese coast. The shoreline was adopted as a proxy to study beach evolution in response to nourishment and to wave forcing. To achieve this aim, images collected by a video monitoring system were used. A nourishment calendar was drawn up based on video screening, highlighting the different zones and phases where the works took place. Over the six-month monitoring period, a total amount of 25 video-derived shorelines were detected by both manual and automated procedures on video imagery. Nourishment works, realized in summer, enlarged the emerged beach extension by about 90 m on average. During winter, the shoreline retreated about 50 m due to wave forcing. Spatial analysis showed that the northern beach sector was more vulnerable and subject to erosion, as it is the downdrift side of the groin.

Key-words: beach; nearshore; remote sensing; erosion; sand.

[Página deixada intencionalmente em branco.]

Resumo

A alimentação artificial de praias é uma intervenção de engenharia que abastece a costa com sedimentos, por forma a aumentar a área de lazer da praia, assim como diminuir a vulnerabilidade à erosão costeira. Este estudo apresenta a avaliação preliminar dos trabalhos de alimentação artificial efetuados na costa portuguesa, dominada por ondas de alta energia. A *shoreline* foi adotada como um *proxy* para estudar a evolução das praias, em resposta à alimentação artificial e à ação erosiva das ondas. Para tal, foram utilizadas as imagens recolhidas por um sistema de vídeo monitorização. Com base nos vídeos recolhidos, foi elaborado um calendário das atividades de alimentação artificial, destacando as diferentes fases e zonas em que as atividades decorreram. Adicionalmente, durante o período de monitorização de seis meses, 25 *shorelines*, derivadas das imagens de vídeo, foram detetadas, de acordo com procedimentos manuais e automatizados. Os trabalhos de alimentação artificial, realizados no verão, ampliaram a extensão da praia emersa, em média, 90 m. Durante o inverno, a *shoreline* recuou cerca de 50 m, como consequência da ação erosiva das ondas. A análise espacial da evolução da extensão emersa da praia revelou que o setor norte da praia em análise é mais vulnerável à erosão, uma vez que se encontra a jusante do esporão.

Palavras-chave: praia; nearshore; deteção remota; erosão; areia.

[Página deixada intencionalmente em branco.]

Table of Contents

[Página deixada intencionalmente em branco.]

Figure Index

[Página deixada intencionalmente em branco.]

1. Introduction to the Dissertation

1.1. Framework

Coastal areas are extremely complex and dynamic environments, which are constantly under change, due to the interaction between atmospheric, hydrodynamic, and sedimentary processes (Pugliano et al., 2019; Thurman and Trujillo, 1999). These areas are, therefore, daily exposed to dynamic natural processes and anthropogenic interventions – such as sand mining, urbanization, and tourism –, which translate into erosion and accretion of coastal areas, causing changes in the long and short term (Aedla et al., 2015; Kermani et al., 2016).

Approximately two-thirds of the world's population inhabits in coastal regions and, more specifically, about 60% of the Portuguese population lives less than 10 km away from coastal zones (Andriolo, 2018; Baills et al., 2020; Pianca et al., 2015). Additionally, numerous activities – such as sport and leisure activities, fishing and aquaculture, transport and navigation – take place in these areas, securing their high socioeconomic value (Aedla et al., 2015; Andriolo, 2018; Gargiulo et al., 2020).

As beaches occur on practically all coasts worldwide, most countries experience coastal safety problems – thus, becoming necessary to protect beaches and dunes against erosion and flooding events (Kroon et al., 2007; Pianca et al., 2015). These events have, consequently, become more frequent, during the past few years, because of the negative effects of climate change – especially due to the sea level rise and severe storm events (Dewi and Bijker, 2019; Gargiulo et al., 2020; Silva et al., 2017).

As a consequence, different engineering structures have been developed, in order to protect coastal areas. For a long time, eroding coastlines were – and many still are – protected by engineering structures, such as groins, seawalls and breakwaters (Castelle et al., 2009; Thurman and Trujillo, 1999). In fact, about 14% of the Portuguese coast is protected by such artificial structures (Marinho et al., 2019). This approach, however, has been being replaced because – although it provides local relief – it can result in the transfer of the problem from one geographical site to another (Castelle et al., 2009).

Subsequently, ever since the 1920s, beach nourishment has become a popular beach management technique for the protection and restoration of coastal areas – especially near urban areas, where erosion episodes are more frequent, due to intense tourism activity (Castelle et al., 2009; Harley et al., 2014; Karambas and Samaras, 2014; Marinho et al., 2019; Semeoshenkova and

Newton, 2015). Beach nourishment consists in the injection of substantial quantities of sediments into the beach system, to extend, widen and elevate the emerged beach area (Chiva et al., 2018; Karambas and Samaras, 2014; Luo et al., 2016). The sediments added to the beach lead to the strengthening of the shore and coastline against storm surge, helping with the wave energy dissipation during storms as well (Karasu et al., 2016). The quality of the sediments to be added on the beach needs to the evaluated, so as to avoid cross-contamination by pollutants (Pinto et al., 2018). Additionally, beach nourishment increases the recreational beach area, which has positive consequences in tourism (Ludka et al., 2018; Silva et al., 2017).

The advantages resulting from beach nourishment works, however, start diminishing over time – leading to the need for further nourishment, to maintain a healthy beach system (Harley et al., 2014). In fact, as the nourishment works finish, changes start occurring quickly – often leading to social criticism, especially when the beach volume decreases rapidly (Pinto et al., 2018). An artificial nourish usually lasts between 3 to 10 years, and the time interval between the sand injection and the loss of 50% of the initially injected sand volume is denominated the half-life period – and can be used as a measure of the longevity of the works (Pinto et al., 2018).

In order to evaluate the effectiveness of nourishment works, it is essential to monitor the beach evolution in response to the intervention, with particular focus on the impact of wave forcing (Mahabot et al., 2017; Semeoshenkova and Newton, 2015; Silva et al., 2017). Moreover, the shoreline's variability reveals helpful information not only for the environmental control and management of coastal areas, but also for policy making and the design of human intervention (Aedla et al., 2015; Hagenaars et al., 2018; Kermani et al., 2016).

The shoreline is defined as the dynamic interface between land and ocean (Andriolo, 2018; Thurman and Trujillo, 1999). Although this definition is quite simple, it is rather challenging to properly define the shoreline, since its position continually changes through time, as a consequence of cross-shore and alongshore sediment movement in the littoral zone, as well as because of the dynamic nature of water levels – induced by wave activity, tides, storm surge, runup, among others (Aedla et al., 2015; Boak and Turner, 2005; Coelho, 2005). Because of this, the shoreline must be considered in a temporal sense – the time scale chosen depending on the specific context of the investigation (Aedla et al., 2015; Boak and Turner, 2005). These characteristics make the shoreline the most common monitoring coastal indicator in morphodynamic studies, as it reveals helpful information on beach variation, being useful for coastal zone monitoring after nourishment interventions (Dewi and Bijker, 2019; García-Rubio et al., 2015; Hagenaars et al., 2018).

There are a variety of different data sources available to determine the shoreline position, as well as to study its evolution – with different degrees of spatial, temporal and image resolution (Angnuureng, 2016; Boak and Turner, 2005). Historical landbase photograph usually gives no information about the sea condition (tide and waves), although it is frequently used to map past shorelines; aerial photography gives good spatial coverage of the shore, but its temporal coverage is very specific; beach surveys can be an accurate source of shoreline information, but the information they provide is limited both spatially and temporally, as a consequence of the high costs associated with the labor intensive method of sending survey teams into the field to obtain data; GPS shoreline, by using kinematic differential GPS, is a fast, low-cost and highly accurate shoreline detection method – the major errors associated with it being the user-selection of the shoreline to be studied; more recently, remote sensing techniques have been becoming increasingly popular, especially because they allow for the coverage of vast areas in quasi-instantaneous periods of time, although sometimes in a quite logistically challenging and expensive way (Boak and Turner, 2005; Holthuijsen, 2007; Pianca et al., 2015; Valentini et al., 2017a).

The advance of digital imaging technologies has made it possible for new remote sensing techniques to be developed – video monitoring techniques being a major example of this (Andriolo, 2019). These littoral video monitoring techniques became popular, since nearly any nearshore phenomena that can be visually identified, can also be quantified by image processing techniques (Andriolo et al., 2020; Archetti et al., 2014; Silva, 2014). Video-imaging techniques are one of the most popular remote sensing techniques to study shoreline evolution, since they have the capacity to detail changes in coastal systems, as well as to provide long-term shoreline change information (Boak and Turner, 2005). In fact, by keeping continuous records of the shoreline, it is considered the perfect technique to study the shoreline's dynamic evolution – especially in the months following a beach nourishment (Harley et al., 2014). This technique materializes when the optical devices are installed on a fixed platform, with a direct view of the shore – then composing a video monitoring station (Andriolo, 2019; Taborda and Silva, 2012).

ARGUS was the pioneer video monitoring system, and, as such, it was the first scientific program to video monitor coastal areas and support coastal studies – by means of video and image processing tools, used to monitor and measure the physical and morphodynamical changes registered on the littoral (Holman and Stanley, 2007; Silva, 2014). The ARGUS System was the result of work developed by the Coastal Imaging Lab (CIL) of Oregon, between the late 80s and early 90s, and has, ever since, created a worldwide network of video-cameras (Holman and Stanley, 2007).

This video monitoring technique has been immensely used over the past few years, as an instrument to monitor and evaluate numerous topics, other than the shoreline, such as: coastal morphology, swash processes, coastal vulnerability assessment, near shore bar morphology, longshore current, surf zone bathymetry, among others (Archetti et al., 2014; Kroon et al., 2007).

The shoreline evolution – as well as other coastal monitoring indicators examined with this technique – can be studied by analysing three specific products: snapshot, Timex, and Variance images, which will be further developed on the next sub-chapter.

1.2. Functioning of video monitoring systems

The video-monitoring cameras, which are part of the monitoring station, are usually installed at an elevated position, in order for them to cover as much of the area to be monitored as possible (emerged beach and nearshore) – knowing one camera covers approximately 2400 meters (Andriolo, 2019; Andriolo et al., 2020). Nevertheless, the station can have more than one video-camera, especially if the area to be monitored is larger (Andriolo, 2018). The video-cameras are also usually connected to a computer – which has control over the image and video acquisitions (Vousdoukas et al., 2011).

Before – and during – the installation of the video-camera (or cameras) it is necessary to study the area to be monitored, in order to ascertain the number of video-cameras to install and the ideal and correct location for the video monitoring station installation (Archetti et al., 2014). Moreover, it is fundamental to study the existence of pre-existing infrastructures that may serve as support for the video-cameras to install. If no pre-existing infrastructures are available, it is possible to build new structures solely for the purpose of bearing a video monitoring station – always pre-assessing the impacts these will produce (Archetti et al., 2014).

The image collection frequency, as well as the data sampling interval, depend on the camera properties and of the aim of the research (Andriolo, 2018). More specifically, they depend on the data storage space, image quality and image processing computational time (Taborda and Silva, 2012). Therefore, according to the different goals of the research, the acquisition rate can vary as follows:

1. One frame per second (1 Hz) usually for a long-term monitoring of shoreline change.
2. Two frames per second (2 Hz) usually for studying swash processes.
3. Ten frames per second (10 Hz) usually for video-measuring high frequency processes, such as overwash.

Nonetheless, for monitoring the shoreline position evolution, higher acquisition rates can be chosen (Valentini et al., 2017a).

Coastal video monitoring operates specific optical products, used for different purposes. These can be snapshot, Timex, Variance (SIGMA), Day Timex and Timestack (Brignone et al., 2012).

Snapshot pictures are simple pictures of the area being monitored. Although these pictures offer little quantitative information, they can still describe the environmental conditions of the beach and are, therefore, used for qualitative visual assessment (Holman and Stanley, 2007; Valentini et al., 2017a).

Timex – or time exposure – images are another product associated with video-monitoring stations. Timex images are digitally averaged image intensity pictures obtained over a pre-defined and fixed acquisition time (usually 10 minutes) – meaning they are the result of processed and superimposed snapshot images over an acquisition cycle (Andriolo, 2019; Angnuureng, 2016). In fact, these images represent the mathematical time-mean of all the frames collected within a period of sampling (Andriolo et al., 2020; Holman and Stanley, 2007).

The fact that these images are digitally averaged means certain moving features – such as waves breaking in the surf zone, as well as other aleatory transitional conditions – are averaged out, by deleting the runup height variability, returning only their mean brightness (Andriolo, 2019; Splinter et al., 2018). This results in the delimitation of the areas of favored wave breaking in the surf zone as white bands, whereas the non-moving objects onshore are rendered exactly as they appear on the corresponding snapshot (Andriolo, 2018; Angnuureng, 2016).

Because Timex images show the variation in pixel color intensity – allowing for a better distinction of beach morphological features –, they are an excellent and frequently used instrument to emphasize submerged sand bar topography, intertidal beach profile, intertidal beach slope, morphology formations on beach face, shoreline, among others (Brignone et al., 2012). In order to minimize errors due to sea level variations, the images used are averaged over short periods of time (30 s) – which is something that expressively improves the accuracy of the shoreline determination (Pugliano et al., 2019; Vousdoukas et al., 2011).

Another product are Variance – or SIGMA – images. Although very comparable to Timex images, there are still major differences between them: while the latter are obtained as the time mean of image intensities from all the frames collected in the aforementioned pre-defined and fixed acquisition time, Variance images are generally stored and presented in terms of standard deviations, for that same period of time (Guedes et al., 2011; Rigos et al., 2016).

Despite their name, Variance images are not actually created by computing real mathematical variance of the individual images collected during the sampling period – but they are generally stored and presented in form of standard deviation (SIGMA), as mentioned before (Holman and Stanley, 2007). Nonetheless, the shorter name (Variance images) prevails for convenience (Holman and Stanley, 2007).

These images enhance the contrast already achieved by processing Timex images (Pearre and Puleo, 2009; Simarro et al., 2015). They allow for a better recognition of submerged foreshore, as well as of regions going through changes throughout the acquisition period, as Variance images are presented in a greyscale palette, being brighter on areas where there is a larger temporal variability – like surf zones –, and darker on the unchanged areas of the beach, such as the dry beach (Rigos et al., 2016; Simarro et al., 2015).

Both Variance and Timex images are frequently used for shoreline contour detection, by delineating the surf zone and wave breaking regions – as they both represent a simple, yet robust, way of synthetizing pixel intensities over the acquisition time period (Andriolo, 2019; Holman and Stanley, 2007).

Daily Time Exposure images (or day-Timex) are another variation of Timex images. These are obtained as a result of averaging all Timex images recorded during one day (Brignone et al., 2012; Holman and Stanley, 2007). In day-Timex, both the tidal dependencies and the light intensity variation due to the sun's angle changing throughout the day are removed (Brignone et al., 2012).

To conclude, there are also Timestack images. These images are the result of sampling a single line of pixels, at a specific location in the image – usually the surfzone (Pereira et al., 2011). The array of optical intensity is generated during the acquisition period – which, as mentioned before, depends on the aim of the study, but is usually around 10 minutes – and is then concatenated according to the frame acquisition frequency (Andriolo, 2018; Pereira et al., 2011).

In essence, single wave transformation processes can, indeed, be recognized on Timestack images and the variation in pixel brightness translates different types of waves (Matias et al., 2019). Furthermore, on these images, the white foam of breaking waves is usually visible as a white stripe, in form of high intensity white pixels (Andriolo, 2019; Matias et al., 2019; Pereira et al., 2011). The variation of the pixel intensity values allows the delimitation of the different zones at the beach (shoaling surf zone, outer/inner surf zone, surf-swash zone, swash zone-dry beach, among others) (Andriolo, 2018).

1.2.1. Modules of a low-cost video monitoring system

The majority of the video systems encompass four major modules: image acquisition, geometry correction and image processing and feature extraction – being followed by image publication –, as seen on Figure 1 (Archetti et al., 2014; Taborda and Silva, 2012).

Figure 1. Major modules of a video-monitoring system (adapted from Taborda & Silva, 2012; Archetti et al., 2014)

The most recent video-monitoring systems are moving towards becoming more portable and low-cost, as well as more easily installed. For this to happen, and according to the COSMOS video-monitoring system developed by Taborda & Silva, 2012, there are four fundamental steps to be followed:

1. The image acquisition and the image processing modules need to be separated, thus making the system camera independent. This means all types of cameras can be used – even webcams –, reducing the installation costs.
2. The post-processing phase should be divided into two separate modules: geometry correction (lens correction and rectification) and image processing and feature extraction. This makes the system more user-friendly, as it instigates the use of already existing programs – reducing the need to programme.
3. Since, by using low cost video cameras, the precision of the results can be affected, the camera needs to be calibrated before its implementation and installation.
4. Developing a simple and user-friendly interface that allows its usage by non-experts.

Image acquisition

The image acquisition module is only the first step associated with video-monitoring systems, as seen on Figure 1. This module consists of the acquisition of images by the video-camera (Andriolo, 2018). The acquired images are often stored in hard drives at the video-monitoring stations – so they can be collected afterwards. Nevertheless, if the computer containing the hard drive has WiFi or Ethernet access, it is possible to remotely access the acquired images (Taborda and Silva, 2012; Vousdoukas et al., 2011).

Geometry correction

The acquired images need to be projected from distorted pixel dimensions to real-world geographical coordinates, in order to provide quantitative information (Taborda and Silva, 2012;

Vousdoukas et al., 2011). This process is called geometry correction and is, as specified on Figure 1, divided in three distinct phases (camera calibration, image correction and image rectification).

Camera Calibration

The main goal of camera calibration is to determine the actual set of camera parameters capable of describing the mapping between reference coordinates and image coordinates, in order to correct the image's distortion induced by the camera's curvature (Heikkila and Silven, 1997). In fact, in the three-dimensional context of video-monitoring systems, this process consists on the determination of the camera intrinsic parameters (internal geometrical and optical parameters) (Heikkila and Silven, 1997; Taborda and Silva, 2012; Valentini et al., 2017a).

The intrinsic calibration process takes place throughout the camera's installation, and it accounts for the following intrinsic parameters: focal length – which describes the distance from the lens's centre to its focal points –, the image centre (and, therefore, its principal point), and, finally, radial and tangential distortion coefficients (Andriolo, 2019; Valentini et al., 2017a). Usually, only the first two intrinsic parameters are determined during the calibration process, whereas the latter is often determined during the image correction step. For visible cameras – the most frequently used in video-monitoring systems – chessboards are often used for the calibration task (Andriolo et al., 2020; Valentini et al., 2017a).

Camera calibration can be estimated from 15-25 images, captured at different angles, which results in a K matrix, usually expressed as seen on Equation (1) (Rigos et al., 2016; Taborda and Silva, 2012; Vousdoukas et al., 2011).

$$K = \begin{bmatrix} fcu & 0 & u_c \\ 0 & fcv & v_c \\ 0 & 0 & 1 \end{bmatrix} \quad (1)$$

Where fcu and fcv express the focal length in the different directions (measured in pixel units u and v, respectively); u_c and v_c represent the image centre. The K_{12} parameter on the matrix, although expressed as 0, can also sometimes be stated as $\alpha_0 \cdot fcu$, where α_0 expresses the skew coefficient defining the angle between the x and y pixel axes.

Image correction

After calibration, it is necessary to proceed to image correction, which corrects the images' distortion, induced by the camera optics. The distortion can be both tangential and radial, and is often corrected by tools, such as *Rectify Extreme* program, since it can be a quite time-consuming

process (Taborda and Silva, 2012). The image correction process is automatically applied on each image acquired – after its storage, but before the image (geo)rectification process (Valentini et al., 2017a).

Nevertheless, the image correction procedure can be explained with the help of matrixes and equations, as seen both on Equations (2), (3) and (4) (Pearre and Puleo, 2009; Taborda and Silva, 2012; Valentini et al., 2017a).

$$\begin{bmatrix} u \\ v \\ 1 \end{bmatrix} = K \cdot \begin{bmatrix} x'' \\ y'' \\ 1 \end{bmatrix} \quad (2)$$

Where u and v represent the coordinates of a point in the distorted system (in the metric coordinate system); K represents the matrix on Equation (1), also named Camera Matrix; and the $\begin{bmatrix} x'' \\ y'' \\ 1 \end{bmatrix}$ vector corresponds to a normalized point with both radial and tangential distortion. Consequently, x'' and y'' can be explained by Equations (3) and (4).

$$x'' = x'(1 + k_1 r^2 + k_2 r^4 + k_3 r^6) + 2k_3 x' y' + k_4(r^2 + 2x'^2) \quad (3)$$

$$y'' = y'(1 + k_1 r^2 + k_2 r^4 + k_3 r^6) + 2k_3 x' y' + k_4(r^2 + 2y'^2) \quad (4)$$

Where:

- $r^2 = x'^2 + y'^2$
- $x' = \frac{x}{z}$ and $y' = \frac{y}{z}$ and they correspond to normalized and undistorted coordinates
- k_1, k_2 and k_3 are radial distortion coefficients
- k_4 and k_4 are tangential distortion coefficients

Image rectification

Following the image correction phase, there is the image rectification. In this process, the external (or extrinsic) camera parameters – such as camera's position and camera's frame orientation in relation to a certain world coordinate system – are also necessary, in addition to the intrinsic parameters (Heikkila and Silven, 1997).

The image rectification process transforms the originally oblique images in the equivalent vertical rectified images – free from distortions induced by the camera's obliquity (Heikkila and Silven, 1997; Taborda and Silva, 2012). Certain photogrammetric procedures allow for the

transformation from Real World coordinates (X, Y, Z) to image coordinates (u, v), by using collinearity equations. In fact, the entire rectification process is supported by collinearity conditions, which describe the physical model, by representing the geometry between the projection centre (u_c, v_c), the point on image coordinates (u_0, v_0) and the corresponding ground coordinates (X_0, Y_0, Z_0) – as represented on the Pinhole Camera Model on Figure 2 (Valentini et al., 2017a).

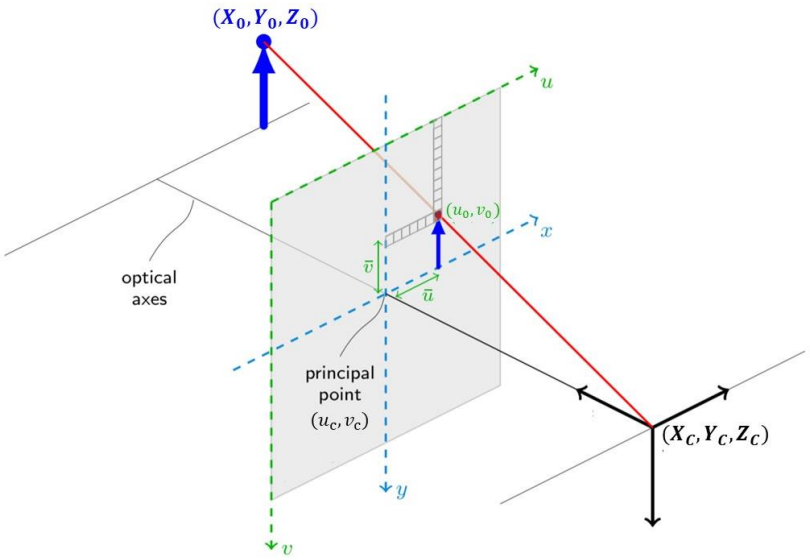

Figure 2. Pinhole camera model (adapted from Valentini et al., 2017)

The physical model (on Figure 2) can also be explained by means of collinearity equations, as represented on Equations (5), (6) and (7). These can be solved by knowing the camera intrinsic and extrinsic parameters – such as the image's principal point (u_c, v_c), focal distance (fc) computed during the calibration procedure, camera position (X_C, Y_C, Z_C) and camera orientation (azimuth α; tilt τ, and roll θ) (the latter two being extrinsic parameters) (Pearre and Puleo, 2009; Taborda and Silva, 2012).

$$u_0 = u_c - f\left[\frac{m_{11}(X_0 - X_C) + m_{12}(Y_0 - Y_C) + m_{13}(Z_0 - Z_C)}{m_{31}(X_0 - X_C) + m_{32}(Y_0 - Y_C) + m_{33}(Z_0 - Z_C)}\right] \quad (5)$$

$$v_0 = v_c - f\left[\frac{m_{21}(X_0 - X_C) + m_{22}(Y_0 - Y_C) + m_{23}(Z_0 - Z_C)}{m_{31}(X_0 - X_C) + m_{32}(Y_0 - Y_C) + m_{33}(Z_0 - Z_C)}\right] \quad (6)$$

Where f represents the focal distance in each respective direction (u and v) and m_{nm} correspond to the parameters of the orientation matrix, M, as expressed on Equation (7) below.

$$\begin{bmatrix} m_{11} & m_{12} & m_{13} \\ m_{21} & m_{22} & m_{23} \\ m_{31} & m_{32} & m_{33} \end{bmatrix} = \begin{bmatrix} \cos(\alpha) & \sin(\alpha) & 0 \\ \sin(\alpha) & \cos(\alpha) & 0 \\ 0 & 0 & 1 \end{bmatrix} \begin{bmatrix} 1 & 0 & 0 \\ 0 & \cos(\tau) & -\sin(\tau) \\ 0 & \sin(\tau) & \cos(\tau) \end{bmatrix} \begin{bmatrix} -\cos(\theta) & -\sin(\theta) & 0 \\ -\sin(\theta) & \cos(\theta) & 0 \\ 0 & 0 & 1 \end{bmatrix} \quad (7)$$

In order to solve the aforementioned equations – and also to estimate the camera external orientation – it is necessary to identify at least 6 Ground Control Points (GCPs), whose real-world coordinates are known, on the oblique undistorted image (Andriolo et al., 2020). These GCPs can be collected by GPS survey and later identified on the acquired images. Similarly, they can also be identified and selected on fixed structures on the coast – like breakwaters, jetties, groins, houses, paths (Andriolo, 2018).

Despite this being a quite frequent presentation of the method used, there is another way of representing the transformation from metric system coordinates (X, Y, Z) to image coordinates (u, v) – as well as vice-versa – through the perspective transformation matrix, $P_{3\times4}$, as seen on equations (8) and (9) (Valentini et al., 2017a; Vousdoukas et al., 2011).

$$P \cdot \begin{bmatrix} X \\ Y \\ Z \\ 1 \end{bmatrix} = \begin{bmatrix} u \\ v \\ 1 \end{bmatrix} \quad (8)$$

Where the P matrix can be decomposed as:

$$P = K \cdot R \cdot [I \mid -C] \quad (9)$$

And where K represents the Camera Matrix, obtained during the calibration procedure, R and C are the rotation and translation matrices of the camera's centre of view (COV), respectively, and, finally, I is the identity matrix.

The C matrix gives the camera's location in the coordinate reference system used, being represented as:

$$C = \begin{bmatrix} X_C \\ Y_C \\ Z_C \end{bmatrix} \quad (10)$$

The R matrix, on the other hand, expresses the COV orientation – defined by three different angles (COV-pan – or azimuth, COV-tilt, and COV-roll), in relation to the cartesian coordinate system, represented on Figure 3.

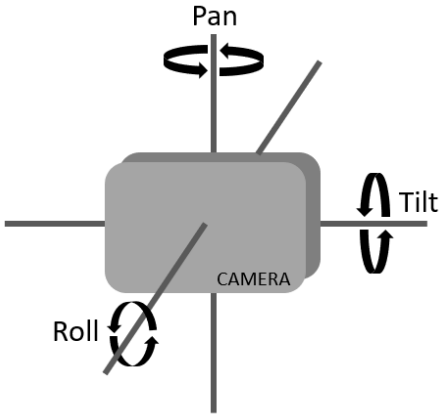

Figure 3. Explanation of the pan, tilt and roll camera movements

The resulting P matrix is a function of the camera angles and coordinates and can be estimated according to an iterative process using GCPs – whose identification criteria has already been specified (Vousdoukas et al., 2011),

For both the image rectification paths, the transformation process of the two-dimensional coordinates is completed by solving either Equations (5) to (7) or Equations (8) to (10). The elevation value, Z_0, however, must be previously defined. In most cases, this value is assumed to be equal to the tidal level recorded during the image acquisition period (Andriolo, 2018),

Even so, the shoreline elevation value can be estimated in a more precise way, according Equation (11) (Vousdoukas et al., 2011),

$$Z_0 = Z_t + \eta_s + Z_{correction} \tag{11}$$

Where Z_t translates the offshore water level, induced by tidal and wind action – but without the contribution of gravity waves; η_s is the wave setup and can be estimated through empiric equations or through numerical models of wave propagation; and, finally, $Z_{correction}$ is an additional correction term, which is estimated differently according to the shoreline detection method used. Additionally, $Z_{correction}$ can be expressed as a function of numerous wave related parameters – such as significant wave height (H_s), deep water wave length (L_0), peak wave period (T_p), among others.

Image processing and feature extraction

The final module before image publication is image processing and feature extraction. With the current video monitoring system development, the image processing techniques are mostly limited to the computation of Timex and Variance images (Vousdoukas et al., 2011).

The feature extraction procedure encourages the use of specific programs, in order to minimise the programming efforts. After the rectification processes have been completed, certain tools (like COSMOS IPT) and other image processing algorithms allow for the creation of rectified and georeferenced image files, which can be directly imported by standard GIS applications(Taborda & Silva, 2012). This is particularly relevant, as many procedures – such as shoreline detection and computation of intertidal beach topography – can highly benefit from GIS capabilities (Vousdoukas et al., 2011).

As this module finishes, the final image product is obtained, leading to image publication, the final module represent on Figure 1.

1.3. Costa de Caparica and beach erosion

Costa de Caparica, located in the Almada Municipality, is a coastal city which represents the biggest and most attractive beach spot of the Lisbon metropolitan area (Duarte et al., 2020). The urban coastal area of Costa de Caparica – comprised between São João beach and Nova Praia beach – has a dense artificialized occupation, with seven groins and a three-kilometre seawall (Duarte et al., 2020; Ferreira, 2016).

Ever since the beginning of its human occupation, Costa de Caparica has been affected by wave overtopping events (Ferreira, 2016). In fact, as seen on Figure 4, the overtopping frequency, for the urban front of Costa de Caparica, is mostly superior to 80%. Additionally, the entire urban front also displays very high values on the hazard index to coastal overtopping events and consequent flooding.

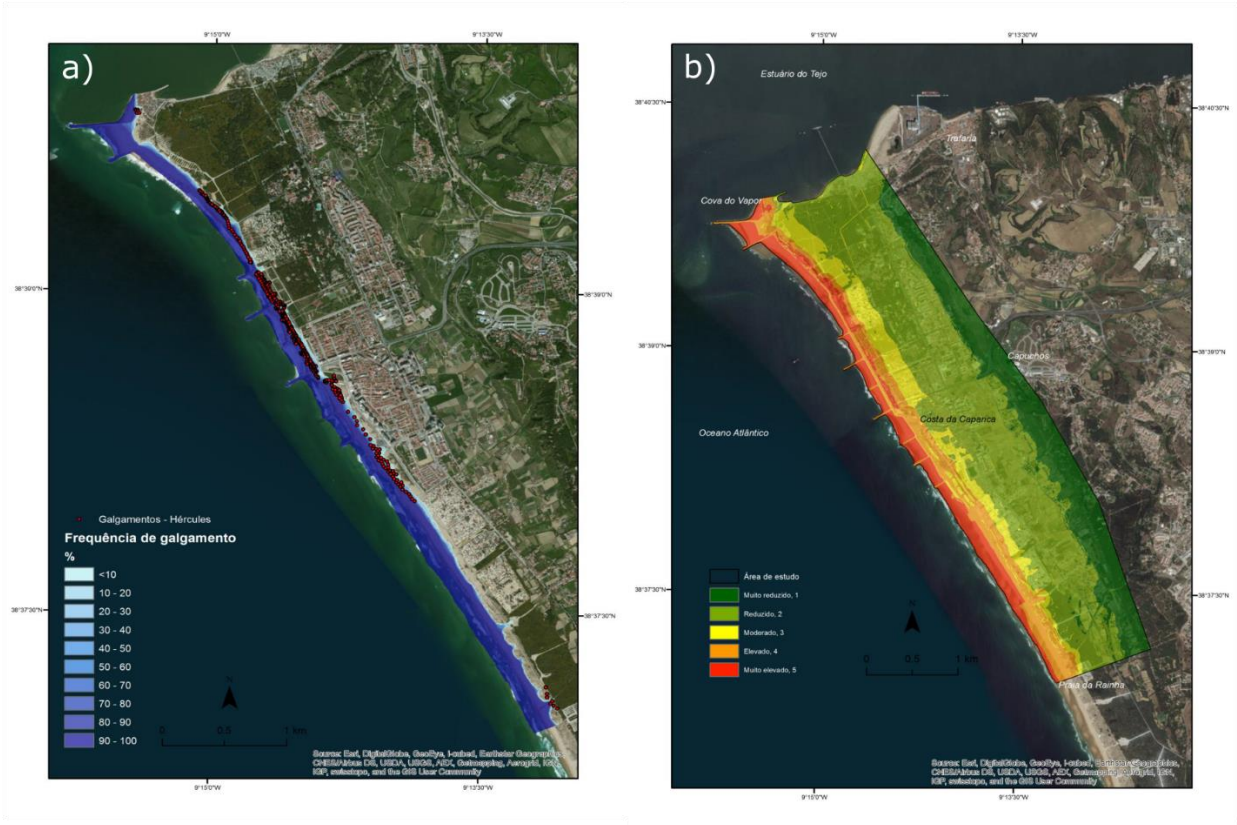

Figure 4. Overtopping in Costa de Caparica. (a) Map with the frequency of overtopping events and flooded areas of the last years (1979-2014), according to the SWAN projection, followed by the projection according to the empirical formula of Stockdon, Holman Howd & Sallgenger Jr. (2006) for 16 beach profiles in Costa de Caparica and with the historical overtopping events of Hercules (2014), and (b) map of the hazard index to coastal overtopping and consequent flooding in Costa de Caparica (Ferreira, 2016).

Associated with the extremely frequent overtopping events, the Costa de Caparica region has been undergoing the consequences of severe erosion since the 1930s, mostly because of significant urban and tourism pressures (Semeoshenkova and Newton, 2015; Veloso-Gomes et al., 2009). Figure 5 shows the hazard index in relation to erosion/accretion for the entire Costa de Caparica, and, although, for the same area, this hazard index is not as high as the one associated with overtopping events, it still displays high values – making the entire area extremely vulnerable to such events.

Figure 5. Map of the hazard index in relation to the erosion/accretion rate (Ferreira, 2016).

Throughout time, there were several coastal management efforts – like the installation of groins –, but after a few years it became clear the area was still very unstable and vulnerable, as severe storms kept affecting the shoreline's position (Agência Portuguesa do Ambiente, 2019; Veloso-Gomes et al., 2009). From 2000 on, the erosion events kept becoming more regular and brutal, making Costa de Caparica the ideal location for this study (Marinho et al., 2019; Veloso-Gomes et al., 2009).

A number of alternatives to hard stabilization infrastructures emerged and were considered, in order to minimize shoreline retreat and infrastructure destruction (Marinho et al., 2019; Veloso-Gomes et al., 2009). In fact, the management strategies stated on the Urban Requalification Polis Program – which determined the shoreline's management plans – started reshaping the already existing groins and sea walls, with consistent nourishment periods (Marinho et al., 2019; Semeoshenkova and Newton, 2015; Veloso-Gomes et al., 2009).

The main goal of these nourishment works is the coastal protection of the vulnerable urban beaches in Costa de Caparica. By increasing the emerged beach extension and elevation of the beaches, as a consequence of the injection of sand into the system, the sea no longer directly affects the shoreline, the dune cord, as well as the spurs and the adherent longitudinal defence – as the swash zone is more distant (Agência Portuguesa do Ambiente, 2019). Therefore, there is a strong reduction on the erosion and shoreline retreat rates, consequently increasing the stability of the beaches (Pinto et al., 2018). Although not the main goal, the recreational beach area also increases with these nourishment works (Agência Portuguesa do Ambiente, 2019).

1.4. Scope and Objectives

This study is part of the ongoing project entitled "To-SEAlert, Overtopping and flooding in coastal and port areas: Tools for a forecast and warning system, emergency planning and risk management" (PTDC/EAM-OCE/31207/2017), which is funded by the Foundation for Science and Technology (FCT). The project's main goal is to develop, implement and validate a series of tools and methods of a WebGIS system, which helps authorities (municipalities, emergency services and civil protection) to monitor, prevent and/or perform activities of extreme weather events, such as coastal overflows and floods in coastal and port areas.

The To-SEAlert project will base its development on two locations in the Lisbon Metropolitan Area: the port of Ericeira and Costa de Caparica. Both sites are known for common flooding and coastal phenomena, damage to people, property, and infrastructure. This project is divided in seven different tasks:

1. Use of satellite images for the historical characterization of wave fields and flooded areas.
2. Integration of video monitoring systems for *in situ* monitoring and characterization of waves, overtopping and flooded areas, and consequent system validation and calibration.
3. Use of physical models to validate the numerical models system.
4. Integration of state of the art numerical models to simulate wave overtopping and flooding.
5. Use of risk assessment methodologies to quantify risks, using multicriteria and probabilistic methods.
6. Assemble an adequate and innovative WebGIS platform to build a decision support tool.
7. To-SEAlert prototypes for Ericeira and Costa de Caparica sites.

This dissertation is integrated on Task 2 of the To-SEAlert project, as it explored the data collected by a shore-based video station at the Tarquínio-Paraíso beach, in Costa de Caparica, on the Portuguese coast, to study the shoreline evolution after a beach nourishment. The main objectives of the present dissertation were to:

1. Elaborate a nourishment calendar based on the video images collected at the monitoring station, to fully detail the nourishment works conducted at the study-site.
2. Monitor the nourishment works and evolution of the emerged beach width during the months following the conclusion of such works.
3. Analyse the preliminary shoreline response to the nourishment works at the Tarquínio-Paraíso beach.

For the latter two objectives, it was fundamental to detect the shoreline position throughout the monitoring period. The shoreline position was detected on a selected subset of Timex and Variance images, following two different methodologies (manual and automated, respectively), and their results allowed for a shoreline evolution analysis from summer to middle winter, in response to wave forcing and consequent high energy episodes.

The shore-based video station – which was installed specifically for the To-SEAlert project purposes, on the roof of the Tryp Lisboa Caparica Mar Hotel, overlooking the study site – has been storing high-resolution images since August 2019.

1.5. Structure

This dissertation consists in the elaboration of a scientific article, submited to *Water*, a peer-reviewed open access journal on water science and technology. The article has already been submitted, accepted, and published (on 06th June 2020).

This dissertation is divided into five chapters: the current one, where the introduction of the work is made – also presenting the scope and structure; the second chapter, which presents part of the methodological procedure of the manuscript version of the article; the third chapter, which includes a conclusion, displaying the limitations and future developments of the work; the fifth chapter, citing the bibliography used; and, finally, the annexes, where the acceptance certificate to *Water* and the formatted accepted article is presented.

[Página deixada intencionalmente em branco.]

2. Manuscript of the Article

In this chapter, it is possible to find the scientific article submitted in manuscript format. The article has the following sections: Abstract, Introduction, Methods, Results, Discussion, Conclusion, Acknowledgements, and References. Nonetheless, as the Abstract was already presented, and the References will be included at the end of the document, this chapter only displays the Introduction, Methods, Results, Discussion, Conclusion and Acknowledgements.

2.1. Introduction

Beach nourishment is a soft engineering intervention that consists in the injection and placement of sediments into the beach system, to extend, widen and elevate the subaerial beach (Chiva et al., 2018; Karambas and Samaras, 2014; Luo et al., 2016). The sediments added to the beach reduce the vulnerability to storms and enhance the wave energy dissipation (Karasu et al., 2016). Additionally, beach nourishment increases the recreational beach area, leading to positive consequences in tourism (Ludka et al., 2018; Silva et al., 2017). In order to evaluate the effectiveness of nourishment works, it is essential to monitor the beach evolution in response to the intervention (Mahabot et al., 2017; Semeoshenkova and Newton, 2015; Silva et al., 2017).

The shoreline, defined as the dynamic interface between land and ocean, is the most common monitoring coastal indicator in morphodynamic studies (Andriolo, 2018; Boak and Turner, 2005; Thurman and Trujillo, 1999). As the shoreline constantly changes due to cross-shore and alongshore sediment movement in the littoral zone, as well as because of the dynamic nature of water levels, it reveals helpful information on beach variation, being useful for coastal zone monitoring after nourishment interventions (Brignone et al., 2012; Dewi and Bijker, 2019; García-Rubio et al., 2015; Hagenaars et al., 2018).

Over the last three decades, shoreline evolution has mostly been studied by remote sensing techniques, namely satellite and shore-based video stations. Satellite imaging is a suitable tool for updating shoreline maps, since they provide long-term observations of coastline changes over regional and national scales (Chen and Chang, 2009; Holthuijsen, 2007; Ponte Lira et al., 2016; Sánchez-García et al., 2017; Vos et al., 2019a, 2019b). Nevertheless, shoreline from satellite can be retrieved with low time frequency, and tidal information at the time of image acquisition is often missing.

In contrast with satellite images, coastal video monitoring provides high-frequency, high-quality and continuous images of the nearshore area (Andriolo et al., 2019; Splinter et al., 2018). Shore-based video systems are composed by optical devices installed on an elevated position

observing the nearshore area. The continuous acquisition of images allows the observation of the dynamic changes of the nearshore, including the shoreline, in order to build a long-term dataset for a detailed description of coastal morphodynamic evolution (Andriolo et al., 2019; Holman and Stanley, 2007; Splinter et al., 2018).

Coastal video monitoring operates specific optical products: Timex and Variance images. Timex are digitally averaged images, collected over a period of sampling (generally 10 minutes), which smooth out the moving features (Andriolo et al., 2019; Angnuureng, 2016; Archetti et al., 2014). Variance images are built instead as the standard deviation of the sampled period, showing with bright pixels the areas with larger temporal variability, and with dark pixels the unvaried areas (Andriolo et al., 2019; Guedes et al., 2011; Vousdoukas et al., 2012).

Due to their properties, Timex and Variance images have been widely used to detect shoreline, as they smooth the water movement on the beach face (Aarninkhof et al., 2003; Archetti and Zanuttigh, 2010; Bracs, 2016; Brignone et al., 2012; Brodie et al., 2019; Osorio et al., 2012; Plant and Holman, 1997; Simarro et al., 2015; Splinter et al., 2011; Uunk et al., 2010; Valentini et al., 2017a, 2017b; Vousdoukas et al., 2011). However, the number of video imagery applications to monitor coastal nourishment is scarce (Brignone et al., 2008; Elko et al., 2005; Harley et al., 2014; Ojeda and Guillén, 2006). Harley et al., 2014 analysed shoreline evolution in response to a gravel beach nourishment in the Adriatic Italian coast, with focus on coastline rotation and recession in response to storm events. M. Brignone et al., 2008 aimed to test the feasibility of a webcam to evaluate the efficiency of a nourishment project carried out on a gravel beach at the Tyrrhenian coast (Italy). Ojeda & Guillén, 2006 studied the sandy nourishment in two artificially embayed beaches on the Spanish Mediterranean coast, while Elko et al., 2005 applied video imagery to monitor nourishment evolution southern an inlet split in the west coast of Florida, facing the Gulf of Mexico. All these works quantified the effectiveness of nourishment works in extending the beach area, however they were conducted at low-energy and micro-tidal systems, where storms play a major role in shaping the coastline.

The main objective of this work was to monitor the nourishment works and to analyse the preliminary shoreline response on Tarquínio-Paraiso beach, a sandy shore in the high-energy meso-tidal Portuguese Atlantic coast. A shore-based video monitoring station was installed on a hotel roof-top and has been storing high-resolution images of the study site. The collected videos during the nourishment works were visually screened to draw up the nourishment calendar, spatially and temporally locating the three phases of works. The rectified Timex and Variance images were used to detect the shoreline manually and automatically, respectively, over the monitored period of six

months. The built shoreline dataset was analysed to quantify the evolution of the emerged beach width in response to nourishment, completed in summer, and further to winter high-energy events.

This study constitutes the first analysis of shoreline variation at the study site. Moreover, the automated shoreline detection and a video-derived breaking wave height technique were tested to set the ground for an automated video-based integrated system capable of describing hydro-and morphodynamics of the Tarquínio-Paraíso beach.

2.2. Methods

2.2.1. Study site and video station

Costa de Caparica is a sandy stretch located on the south margin of the Tagus river estuary, on the central Portuguese coast (Figure 6a). This area represents the main site for coastal recreational activities of the Lisbon and Setúbal regions (Junta de Freguesia Costa de Caparica, 2019). The area has experienced coastline retreat of about 200 m in the last 50 years, resulting in more exposition of the urban front to severe storm events (Marinho et al., 2019; Silva et al., 2017; Veloso-Gomes et al., 2009). In order to protect the urban front, periodic nourishment operations are performed at Costa de Caparica (Agência Portuguesa do Ambiente, 2019; Marinho et al., 2019). In 2019, the nourishment activities took place between the 13th August and 24th September. A total sand volume of 1,000,000 m^3 was distributed on the seven beaches of Costa de Caparica, between the northernmost São João beach and the southernmost Nova Praia beach (Agência Portuguesa do Ambiente, 2019).

The study site is the Tarquínio-Paraíso beach (38°38'30.3"N, 9°14'20.5"W), the fourth urban beach in Costa de Caparica (Figure 6). The beach extends for about 390 m longshore, with NW-SE orientation, and it is limited sideways by two groins, and landward by a seawall. The site is characterized by a mesotidal tidal regime, where the average tide amplitude is 2.10 m, and its maximum elevation is 4 m. The wave regime has an average significant height of 2 m, and periods between 7-15 s, predominantly coming from Northwest (Andriolo, 2019; Dodet et al., 2010). The nourishment activities occurred between 26 August and 4 September 2019, with about 140.000 m^3 of sand placed on the shore (Agência Portuguesa do Ambiente, 2019). The grain size of the nourished sand (D_{50}=0.55 mm) matched the characteristics of the native sand (Agência Portuguesa do Ambiente, 2019).

To characterize the topographic changes, a cross-shore beach profile was surveyed with RTK-GPS instrumentation prior and after the nourishment works over six months, on the location represented on Figure 6c and Figure 6d.

Tidal data was obtained by the tide gauge of Cascais (38.69ºN, 9.42ºW) (ftp://ftp.dgterritorio.pt/Maregrafos/Cascais_radar/2019/), while Hindcast wave and wind hourly data were provided by Puertos del Estado, a state-owned Spanish company with headquarters in Madrid (http://www.puertos.es, SIMAR), at the most representative SIMAR point (38.50ºN, 9.50ºN) (Figure 6b).

Figure 6. Study site map. a) location of Costa de Caparica; b) location of Tarquínio-Paraíso beach (circle), Cascais tide gauge (triangle), and SIMAR point (square); c) location of the video-station (in green) and of the cross-shore profile surveyed over the monitored period (orange, see Section 2.3.2.); d) Timex image, and e) Variance image.

A video-monitoring system, comprising an Internet Protocol Vivotek IB9365-HT camera, was installed on a hotel rooftop at 90 m above mean sea level (MSL), looking at the Tarquínio-Paraíso beach, on 30 July 2019 (Figure 6c). The system has been acquiring video-images at 2 Hz, continuously during daylight hours, recording 15 hours per day. In this work, the data used was continuously collected over six months, between 1 August 2019 and 31 January 2020. Overall, the

dataset consisted of 126 days, as video data was lost between 14 November 2019 and 10 January 2020.

The video imagery dataset was corrected by the lens-inducted distortions following the Bouguet procedure (Bouguet, 2015). Subsequently, 10-minute Timex (Figure 6d) and Variance (Figure 6e) images were produced and rectified at the tidal level corresponding to the acquisition time. The rectification procedure was based on collinearity equations (Pearre & Puleo, 2009; Taborda & Silva, 2012; Valentini, Saponieri, & Damiani, 2017b).

2.2.2. Beach nourishment monitoring

The nourishment works started dredging sand from the bottom of the southern bar channel of the Lisbon port, at about 17 m depth (Agência Portuguesa do Ambiente, 2019).

The dredged sand was transported through submerged metal pipes from the drag suction dredge to the shore, where it was pumped on the subaerial beach and repositioned by caterpillars. This nourishment procedure was considered as the most efficient to avoid the disturbance of fishing boats in the nearshore, and to reduce the environmental impact on the beach (Agência Portuguesa do Ambiente, 2019).

From the collected videos, three main nourishment phases were distinguished (Figure 7):

- the pipe-laying phase, when tubes coming from the dredge boat to the shore were placed (and moved) on the beach;
- the sand injection phase, which consisted in the actual nourishment, when the sand was pumped on the beach;
- the re-distribution phase, when caterpillars redistributed the dredged sand on the beach.

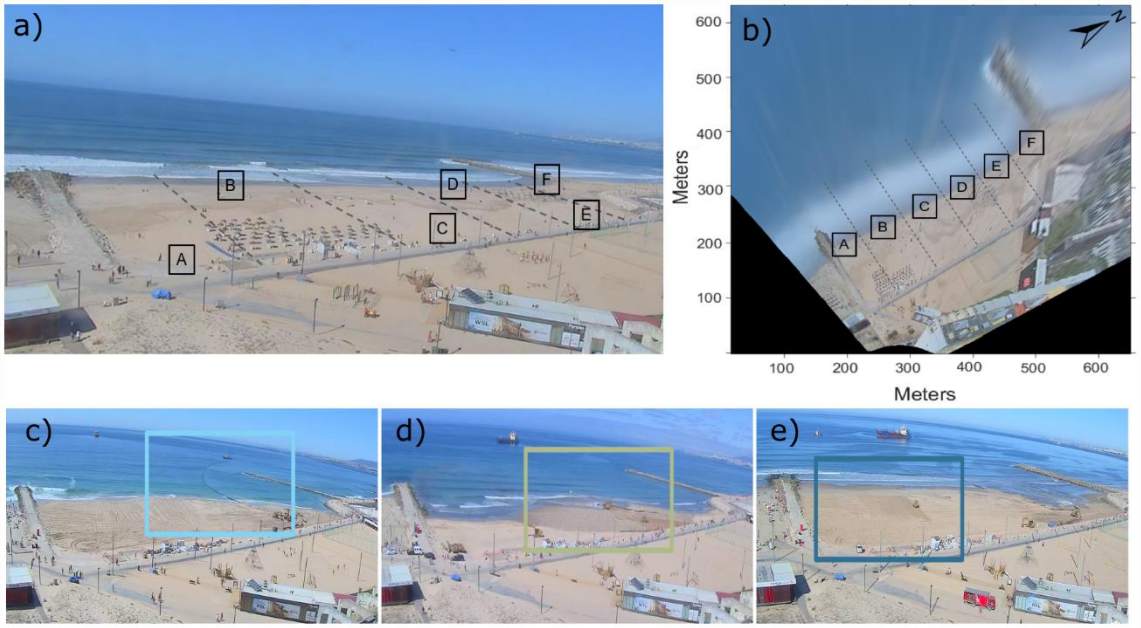

Figure 7. Different nourishment zones and nourishment phases at the Tarquínio-Paraíso beach. a) nourishment zones; b) nourishment zones displayed on rectified image; c) pipe-laying phase; d) sand injection phase, and e) re-distribution phase. The different rectangles indicate the specific area at the beach where each phase is taking place.

Based on the aforementioned definitions, it was possible to elaborate the nourishment map/calendar, identifying the days and zones where the distinct nourishment phases took place. For a regular elaboration, the beach was divided in six different sectors (Figure 7a and Figure 7b), each representing an approximate longshore extent of 70 m.

2.2.3. Shoreline detection

In order to describe the shoreline variation over the monitored period, a series of images was selected to apply manual and automated shoreline detection. Considering the video dataset, a first screening excluded poor quality images deteriorated by dust or rain drops on the lens, and those images acquired during adverse weather conditions or affected by sun glitter. A second criterion was to reject images with crowded beach, as the presence of people on the shore may affect shoreline detection. Finally, among the remaining available video data, images with tidal level corresponding to the MSL were selected (i.e. tidal level within ± 0.02 m), following the procedure proposed by Chang et al., 2019 and Harley et al., 2014. This approach allowed to minimize the influence of tidal variability on the resulting shoreline position, and to compare shoreline positions taken at the same sea level.

Manual shoreline detection

The manual shoreline detection procedure was performed on rectified Timex in Matlab environment. To make the procedure regular, a series of 37 parallel transects, with an offset of about 10 m and perpendicular to the seawall, were superimposed on the image (Figure 8). The

detection process consisted in manually marking the limit between water and dry sand at each transect, interpreted as such by the operator.

The baseline chosen corresponded to the seawall backing the beach. Therefore, the actual cross-shore extent of the emerged beach was found by subtracting the baseline, at each transect, from the shoreline position. The shoreline variation analysis consisted in comparing the shorelines detected over the monitored period.

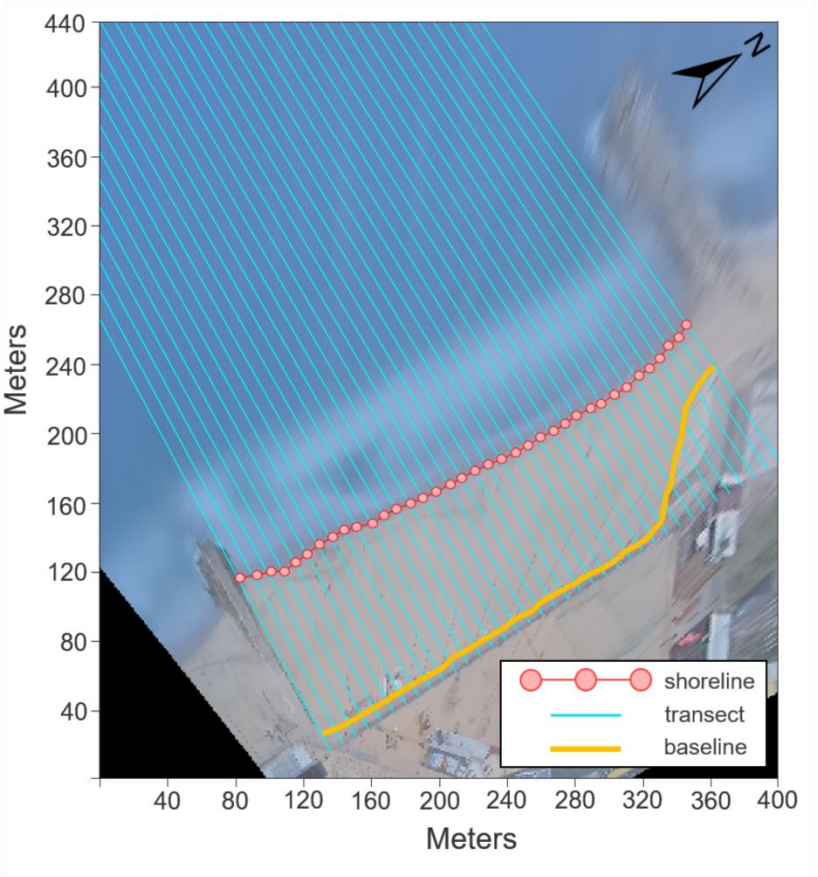

Figure 8. Manual shoreline detection procedure performed in Matlab environment. The red circles indicate the point where each transect intercepts the limit between water and dry sand, and the whole set of 37 points represent the shoreline position. The yellow line indicates the baseline – the position of the seawall, against which the shoreline position will be measured.

Automated shoreline detection

Besides manual detection, a dedicated algorithm was implemented to automatically mark the shoreline. For the automatated detection, Variance images were chosen as principal sources, and the same 37 transects used for the manual detection were exploited for sampling pixel intensity.

Given I_{TX} the pixel intensity sampled on Timex, and I_{VAR} the pixel intensity sampled on Variance on the transects, the steps undertaken by the Matlab-based detection algorithm were the following:

- Masking dry beach. The color ratio Red:Green bands was computed from I_{TX} profile. A conservative value of 1.4 was used to filter out the emerged beach on I_{VAR}, as similarly done in Andriolo, 2019.
- Min–Max normalization of the Blue band of I_{VAR}. The pixel intensity statistical values of I_{VAR} are transformed to the range 0–1.
- Smoothing data. I_{VAR} are smoothed with a moving average window of 10% of the total transect length.
- Masking surf zone. We searched the first peak of I_{VAR} seaward the dry beach limit, which identifies the surf–swash zone boundary (Sw_{min}, as proven in (Andriolo, 2019))
- Detrending. The mean value of I_{VAR} profile, talen between dry beach and swash zone limits is subtracted from the main vector.
- Shoreline detection. The shoreline is identified at the cross-shore location in which I_{VAR} has a null value.

2.3. Results

2.3.1. Hydrodynamics

Figure 9 shows the hydrodynamics during the monitored period. The highest H_s values and the most energetic days occurred between November and January, the main event being in December with the maximum H_s = 7 m. The wave direction varied between 225º and 350º, with predominant Northwest (NW) direction.

Figure 9 also indicates the days chosen for shoreline detection and the days where beach profile surveys were performed. Over the monitored period, the shoreline detection frequency was biweekly. Nonetheless, during the nourishment period, the shoreline was detected daily to describe the evolution of the beach width. Moreover, in November and January, the shoreline was detected weekly, as high energy episodes were more frequent. The topographic surveys represented were performed after the nourishment works over the monitored period to quantify the 3D evolution of beach profile.

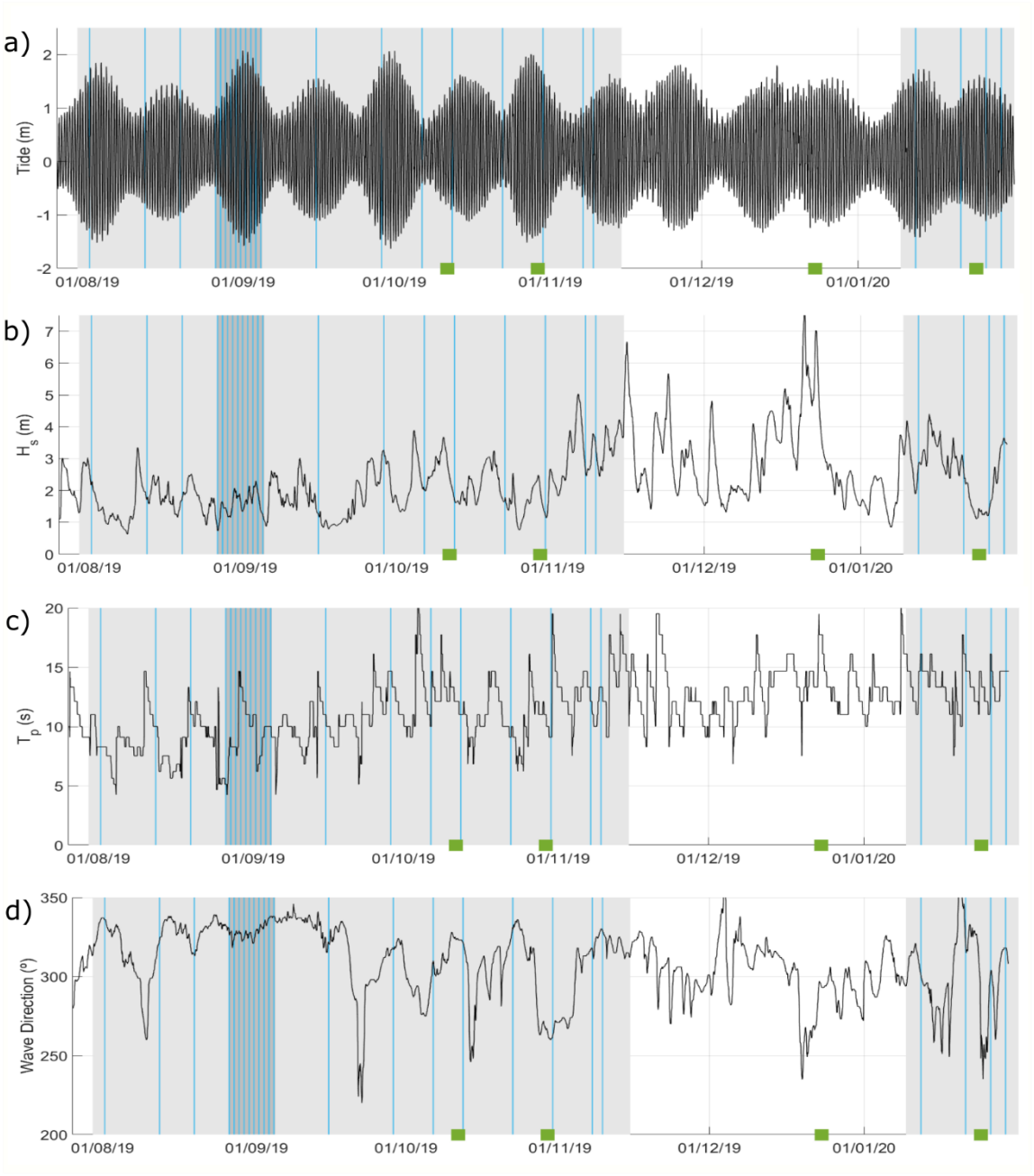

Figure 9. Hydrodynamics of the study site. a) tide level (MSL) from Cascais tide gauge; b) significant wave height, c) wave period, and d) wave direction (from Puertos del Estado). Light gray rectangles indicate the video-monitoring period, blue vertical lines indicate the days chosen for shoreline detection, and the green squares represent the days when topographic surveys occurred.

2.3.2. Beach profile evolution

Figure 10 shows the topographic evolution of the chosen beach profile (see Figure 6c and Figure 6d for location on the beach). The profile of 18 July 2019 corresponded to the beach configuration prior to the nourishment and the monitoring period (slope of 0.035), while the profiles acquired in October were the first-available beach configuration after the nourishment.

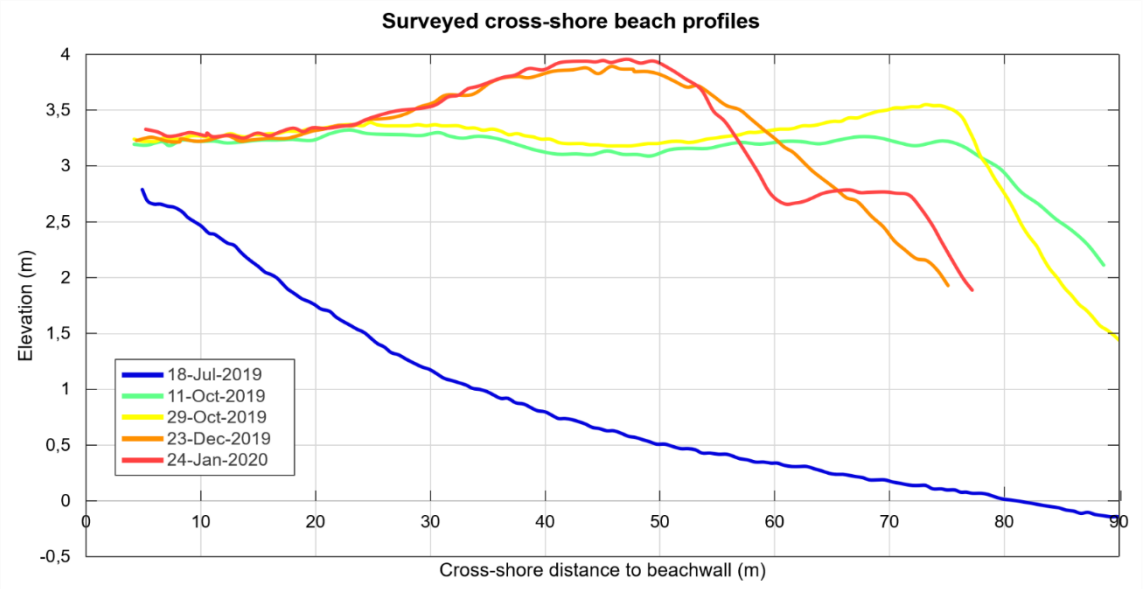

Figure 10. Surveyed cross-shore beach profiles of the Tarquínio-Paraíso beach. The elevation of each profile is reffered to the MSL.

At 60 m location, the slope was inferior to 0.01, showing little variation in elevation between the surveys. After 60 m, the profile showed an increase in elevation of about 0.30 m, when compared with the previous profile, which could be attributed to the deposition of sediments by strong waves registered between 27 and 29 October 2019.

The profile of December displayed a sedimentary elevation of 1 m between the 25 and 60 m locations. There was an increase in the frictional forces between the high energy waves, because of the high energy episodes in December (Figure 9b) and the beach surface, resulting in more sediment deposition in this area. This elevation represented an increase of approximately 27 m^2/m in sand volume, in comparison with October, for that same area. Moreover, on the January profile, while there were no high energy events comparable with the ones from December, according to Figure 9b and the available video data, the sedimentary elevation prevailed. After December, some of the accumulated sediments started being mobilised by wave action, resulting in a secondary berm, at 60 m location.

Considering the surveyed cross-section (Figure 10), the unit beach volumes were estimated as the volume of sand contained in a unit length of the beach, computing the integral of beach profiles. Before nourishment, the unit volume was about 83 m^2/m, and increased to 263 m^2/m after the nourishment works. By the end of the monitored period, in January, the unit volume decreased to 235 m^2/m. The estimation of the total volume of the beach accounted for the longshore extension of 390 m. The total sand volume was approximately 33,000 m^3 prior to the nourishment, over 100,000 m^3 in October, and about 90,000 m^3 in January.

2.3.3. Beach nourishment calendar

The nourishment calendar is shown on Figure 11. The nourishment activities started from the central zone of the beach (zones B and C), and then moved to zones A and D. Finally, on the last days of the nourishment period, the works took place on zones E and F, located on the northern sector of the beach.

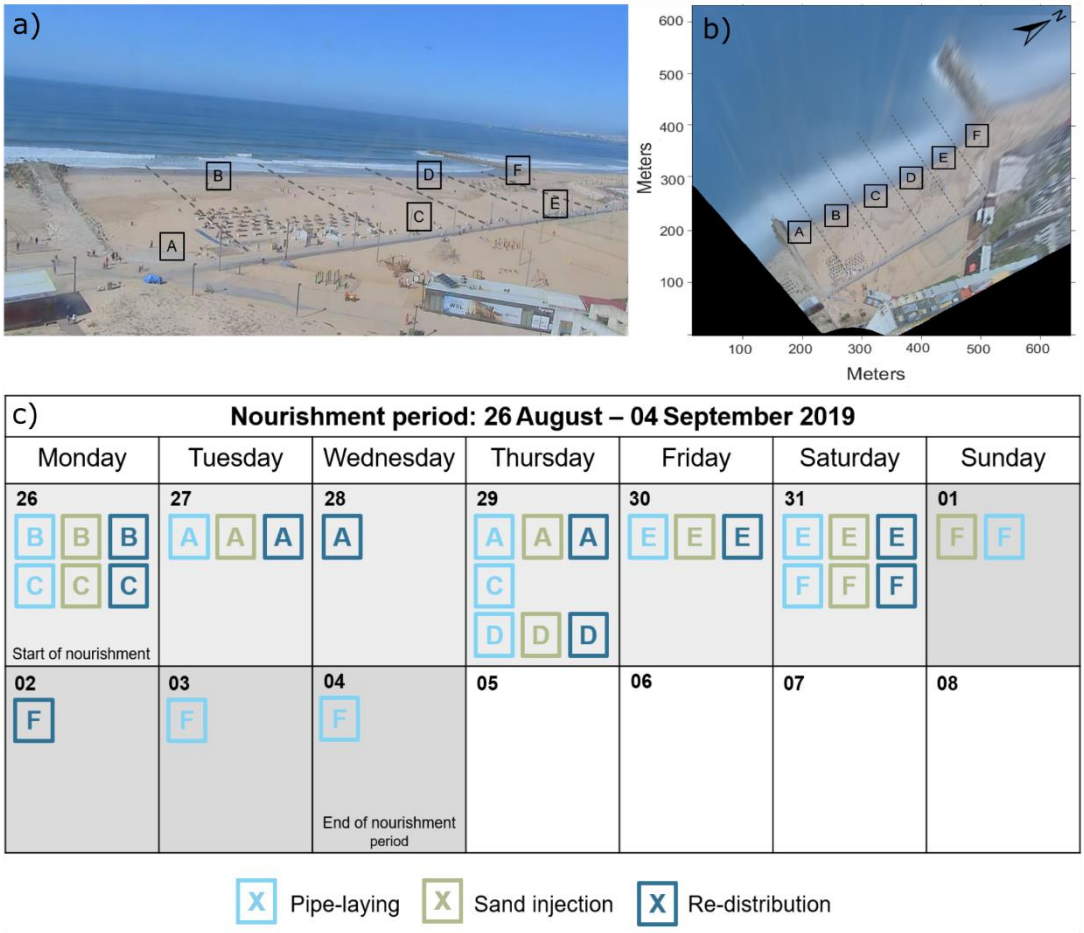

Figure 11. The beach nourishment works calendar for the nourishment period. (a) nourishment zones; (b) nourishment zones displayed on rectified image; (c) the nourishment calendar, indicating the zones where each phase took place, on each day.

The three phases were conducted and completed in each sector (or sectors, if they were being conducted on different zones, at the same time), before moving to the next one. On each different zone, the works were completed in 1-2 days, the exception being zone F. On the last two days of nourishment, the sand injection and re-distribution phases had already ceased, only the pipe-laying phase was still occurring on zone F, as they were already preparing the tubes for the nourishment works on the next beach.

2.3.4. Shoreline variability

The shoreline variation registered over the monitored period is shown in Figure 12 (these results were obtain through the manual methodology). The initial emerged beach extension was inferior to 50 m. After the nourishment works, the shoreline advanced between 80 to 100 m, for the entire longshore extension, resulting in an emerged beach width of 130 m on average. Between November and January, due to high energy wave events, the shoreline retreated over 30 m. It was not possible, however, to analyse the shoreline position evolution during this phase since it coincided with the data loss period. On the last monitored days, the emerged beach extension was about 30 m larger than in August, on average.

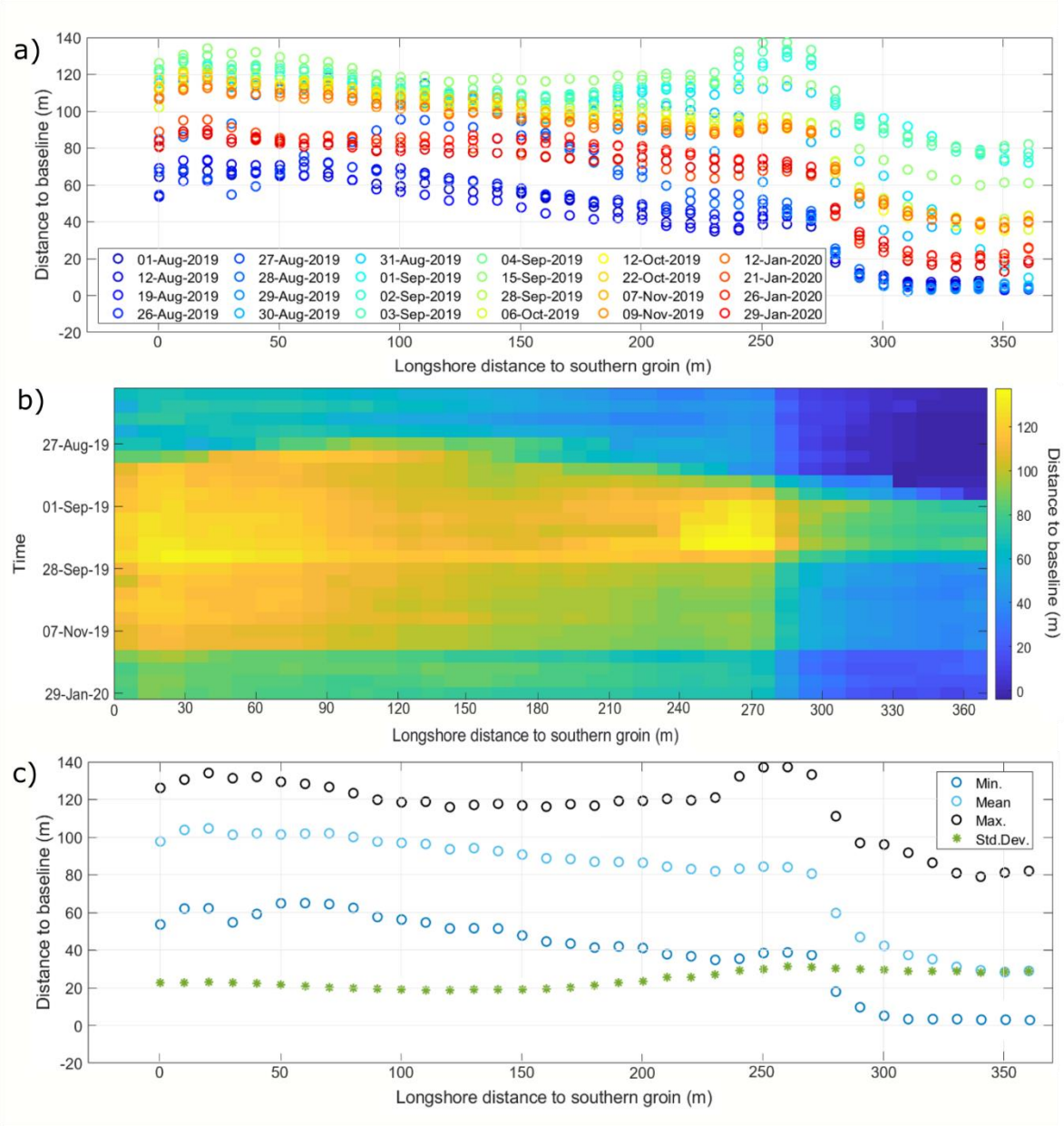

Figure 12. Shoreline position evolution. (a) shoreline evolution through the monitoring period (August-January); (b) timestack image displaying the shoreline evolution, where each row represents a calculated shoreline, and each column represents a transect,

i.e. a longshore distance to the southern groin: (c) the minimum, mean, maximum, and standard deviation values of distance to baseline/beach extension, during the monitored period.

In general, the southern sector of the beach registered the largest emerged beach width, while the northern sector was the area most affected by erosion events, with significant shorter mean beach width (Figure 12c). The standard deviation values reached its peak around 250 m from the southern groin (Figure 12c), as supported by the significant increase in beach extension registered for that same area, during the nourishment (Figure 12b).

2.3.5. Manual *versus* Automated shoreline detection

The relation between manual and automated shoreline is shown on Figure 13. While the results presented on the previous chapter were obtained through the manual methodology, the automated results were satisfactory, with a median disparity of 5 m and an averaged RMSE of 10 m, when compared with the manual technique. Considering the transects, the southern sector was more difficult to retrieve automatically in comparison with the northern sector. This may be due to the lower resolution of the rectified images on the southern sector since it was the furthest from the camera. The detection on northern limit profiles was also affected by some uncertainties, perhaps due to the sampled transects being closer to the groin on rectified images. Here, the sampling algorithm may have been affected by shadow and wave diffraction generated by the groin. Considering the automated shorelines detected over time, it is of interest to note that later shorelines (November 2019 and January 2020) were detected slightly seaward when compared to the manual shorelines (about 5 m on average). During more energetic days, it was more difficult to visually identify the limit between water and dry sand on Timex, as swash excursion was larger and more irregular. In this regard, Variance images are more appropriate to correctly identify the averaged swash (Andriolo, 2019).

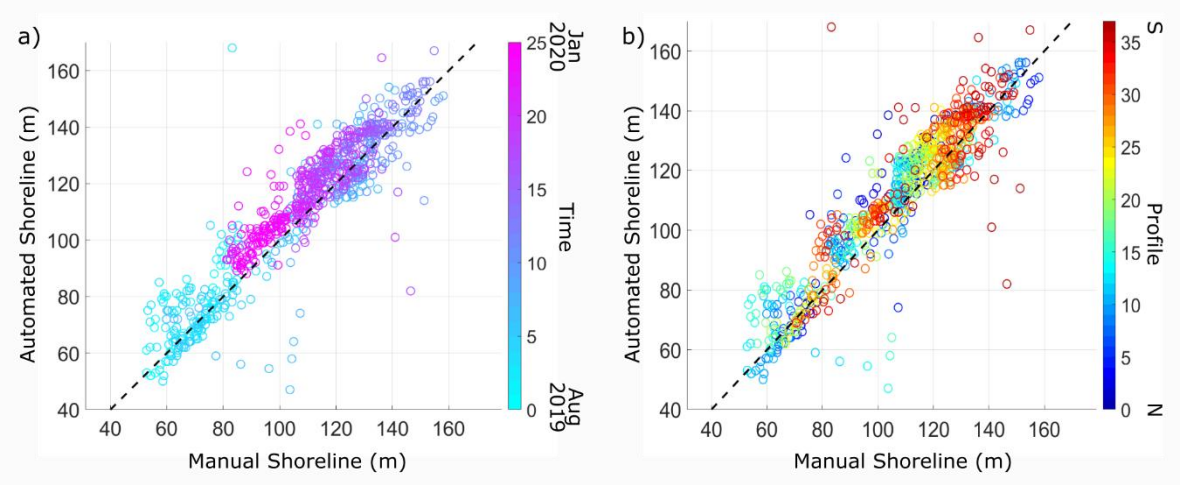

Figure 13. Manual and automated shoreline detection. a) Comparison based on shoreline date; b) comparison based on sampled transect. Dashed black line indicates identity.

2.4. Discussion

In this work, the shore-based video imagery technique confirmed its versatility and suitability to monitor nourishment works and study coastal processes. The beach nourishment calendar (Section 2.3.3) provided a spatial and temporal overview of the procedures, by identifying the different zones and phases of the nourishment works. The example shown in Figure 11 was useful to understand the nourishment dynamics and provides a useful costal management tool for supervising the works on the beach. It is worth noting that in the works monitored by Harley et al., 2014, on the low-energy Adriatic coast, the sediment (mixed gravel) was deposited by the dredger directly on the shore and redistributed by wave action. Since the dredger needed to repeat the action of digging, transporting, and releasing the material several times, nourishment works lasted about 22 days for an embayed beach of 1 km. In this study case, the sand was transported through pipes from the dredgers to the shore and reallocated by caterpillars on the emerged beach. Although the use of machineries may have a negative ecological impact on the beach, this allowed to fasten the works and complete the nourishment of the Tarquínio-Paraíso beach (390 m) in about one week.

The use of continuous video monitoring allowed the detailed quantification of the success of the nourishment project in increasing the extent and area of the emerged beach (Section 2.3.4.). However, the analysis was limited to shoreline advance and retreat, as video imagery did not permit to evaluate the variation of beach volume. It was not possible to distinguish the influence of longshore and cross-shore transports in sediment dynamics. On one hand, the beach orientation (NW-SE) in relation to the predominant wave direction (NW) indicate that longshore current may have a significant impact in shaping the beach, in particular in the downdrift side of northern groin. On the other hand, the limited length of the beach (390 m) suggests that cross-shore sediment transport may play the major role in beach erosion and accretion. Similar constraints related to shoreline-based studies were highlighted by the other authors that used video monitoring technique to evaluate nourishment works (Harley et al., 2014; Ojeda and Guillén, 2006), although these analysis regarded shoreline variation at low-energy Adriatic and Mediterranean coast.

The beach profile analysis (Figure 10) has shown that sand was moved up in the intertidal area by storms during the energetic winter months, when shoreline analysis indicated shoreline retreat of about 30 m in respect to autumn months. The sand on the emerged beach has likely remained in the beach system though, as coastal processes likely redistributed the sand on the shore and perhaps increasing dry beach area. In this regard, further work will increase the frequency of

beach profile surveys and use a longer video dataset to fully evaluate the efficacy and effectiveness of the nourishment performed in summer 2019.

The coastal video station has been installed with the aim of a long-term monitoring of the coastal evolution of the Tarquínio-Paraíso beach, and it is still operative. In this perspective, the automated shoreline detection proposed in this work, similar to Emami et al., 2019, was shown to be reliable and returned adequate resolution, when compared to the manual detection. At the study site, the use of Variance images for developing the automated algorithm was chosen, as the saturated beach may affect and mislead the shoreline detection on Timex (Andriolo et al., 2018; Pearre and Puleo, 2009; Simarro et al., 2015; Valentini et al., 2017b; Vousdoukas et al., 2011). Automated detection also overcomes the subjectivity of the manual procedure, since the identification of the water-sand limit is based on the operator interpretation. Nevertheless, the use of Variance is recommended for detecting the shoreline on an unoccupied beach. The presence of people (beachgoers, fishermen, surfers etc.) and moving objects (tractors, quads etc.) are highlighted on Variance as bright pixels like the swash movement exploited to detect the shoreline. Therefore, a crowded beach negatively affects the automated detection (Andriolo, 2019), whereas on Timex moving effects are smoothed out (Andriolo, 2019; Splinter et al., 2018).

To improve the morphodynamic analysis, the $Hs_{b,v24}$ method (Andriolo et al., 2020) was tested, to estimate the wave height using Timex image (Figure 14). The method is based on the findings that the cross-shore length of the typical time-averaged signature of breaking wave foam on Timex, can be empirically associated with the local water depth at breaking, thus to breaking wave height (Andriolo et al. 2020).

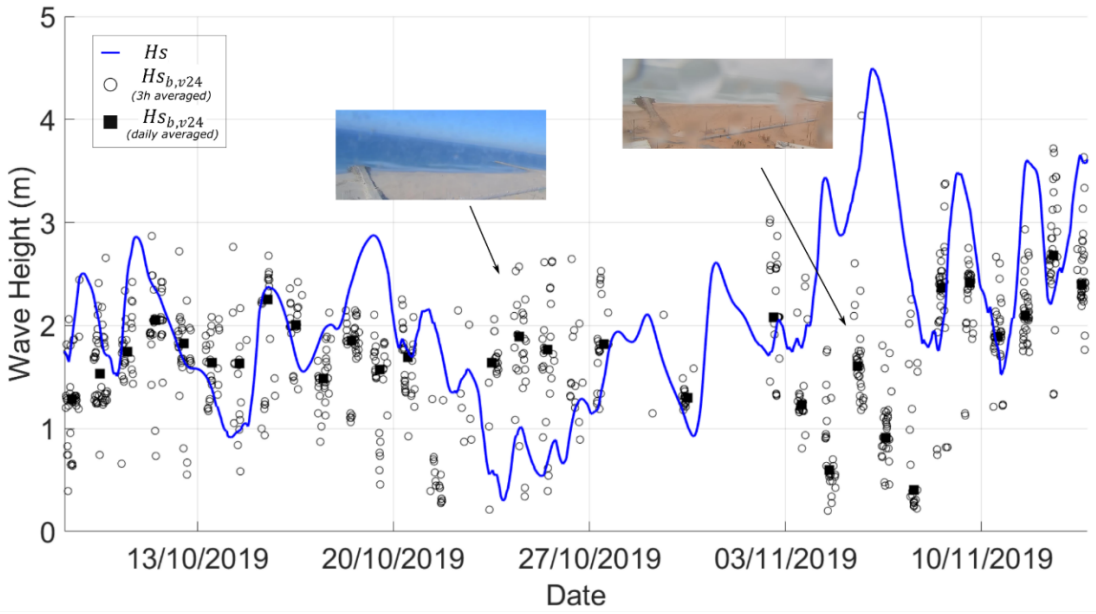

Figure 14. Video-derived breaking wave height $Hs_{b,v24}$ (Andriolo et al., 2020). Insets show two examples of images with dirty lens, rain drops and presence of rip currents in the nearshore, which led to poor results.

A total amount of 35 days, covered by about 3000 rectified Timex, were processed to sample the wave breaking bright pixel pattern over the nearshore bar and eventually applying the $Hs_{b,v24}$ method to retrieve the estimation of breaking wave height for each 10-minute Timex. The video-derived results were 3-hours and daily averaged to be compared to 3-hours offshore wave data available (Section 2.3.1.). Overall, the video-derived wave height had a correlation coefficient of 0.35 with the offshore data. Although the propagation of offshore data, considering period and direction, would have provided a more reliable evaluation of video-results, at this stage it was not considered. The measures were negatively affected by rain drops and dust on the lens, presence of mist and low visibility on the beach (Figure 14). In addition, the fully automated methodology returned poor description of breaking pattern when rip currents were present on the nearshore, as already pointed out by Andriolo et al., 2020. Therefore, an automated algorithm to discard the low-quality images will be developed.

The preliminary test for video-derived breaking wave height is intended to be combined with the automated shoreline detection to build a video-based integrated system that will fully describe the nearshore hydrodynamics and morphology. Besides the breaking wave height and shoreline, the system is expected to provide nearshore bathymetry and hydrodynamics (Abessolo Ondoa et al., 2016; Almar et al., 2011; Andriolo et al., 2019; Thuan et al., 2019; Vousdoukas et al., 2011), wave runup (Almar et al., 2011; Guedes et al., 2011; Senechal et al., 2011), and intertidal topography (Andriolo et al., 2018; Vousdoukas et al., 2011).

2.5. Conclusion

This work evaluated the preliminary shoreline response to a sandy nourishment carried out in the wave-dominated Portuguese coast during summer 2019. In addition, this work constitutes the first high-frequency and high-resolution shoreline changes description at the study site, the Tarquínio-Paraiso beach.

Imagery collected by a coastal video monitoring station was used to draw up the nourishment calendar, and to quantify the emerged beach variation over six-months. Timex and Variance images were used to detect the shoreline, by manual and automated techniques, respectively.

The nourishment calendar showed that the phases of the works, namely pipe-laying, injection and re-distribution of sand, started from the centre of the beach and ended at the northern sector. For each of the six areas chosen to divide the beach, the three phases were usually completed in one day. Overall, the nourishment of the beach, measuring 390 m longshore, was finalized in ten days.

The nourishment works increased the cross-shore beach extension of 90 m on average. During high energy events in autumn, the shoreline retreated about 50 m. After six months, the emerged beach width was about 30 m larger than prior to the nourishment, with a similar longshore configuration. The preliminary analysis of the beach response to the nourishment highlighted that the northern beach sector is the most vulnerable, with rapid beach extension decrease, as it is the downdrift side of the groin. Overall, the beach width increased by the sand supply, preventing the usual flooding occurrences at Costa de Caparica, during high-energetic events, until the end of January.

The automated shoreline detection and video-derived breaking wave height were successfully tested and showed promising results, setting the ground for an automated video-based integrated system that will fully describe the nearshore hydrodynamics and morphology at the study site.

2.6. Acknowledgements

The authors wish to thank Cláudio Macedo Duarte for the fundamental support in the video station installation and management, Ana Nobre Silva and Hugo Teixeira for the help during topographic surveys and image rectification, Rui Taborda for video station installation and project supervision. The authors would also like to acknowledge the Municipality of Almada and the Hotel "TRYP Lisboa Caparica Mar" for the logistical support in the video monitoring system installation.

[Página deixada intencionalmente em branco.]

3. Conclusions and future developments

A low cost video monitoring station was installed at an elevated position of 90 m above MSL, looking at the Tarquínio-Paraíso beach, in order to study the success and evolution of the periodic nourishment works, in response to the increasing wave forcing during autumn and winter months. This study was undertaken by analysing the shoreline position evolution through Timex and Variance images, following both a manual and automated methodology, respectively. Additionally, the present study constituted the first high-frequency and high-resolution shoreline changes description at the Tarquínio-Paraíso beach.

The shorelines identified in the beginning of August showed, throughout its extension, the urgent need for beach nourishment, especially in the northern sector, where the cross-shore sand extension was almost non-existent. After nourishment, the emerged beach width was found to increase between 80 to 100 m, in all transects. However, it started decreasing as autumn began, and the wave forcing episodes became more frequent. A pattern of rapid shoreline retreat was observed, more intensely on the northern sector. This is, however, a direct consequence of groins: sediment erosion takes place directly downstream of the groin, whereas sediment deposition occurs upstream of it. The deposition area coincided with the southern sector of the beach, where the emerged beach width was always superior, and the shoreline retreatment rate was inferior.

The northern sector displayed higher standard deviation values since this area represents one of the two sites where umbrellas are installed during summer. As this sector was the most affected by erosion, it was fundamental to increase its sand volume in a higher proportion, when compared to the remaining sectors. Nonetheless, this increase might have been a consequence of the sediment readjustment on the beach system, after the completion of the nourishment works.

The other site where umbrellas are installed is on the southern sector of the beach, where the standard deviation values were not as high, as this sector was not as affected by erosion. By the end of the monitored period, the overall emerged beach width was getting closer to the one registered on the beginning of August.

Regarding the two different shoreline detection methodologies followed, manual detection performed on Timex proved to be subjective, since the boundary between water and sand was defined based only on the operator's interpretation, and beach saturation may have induced errors and misinterpretation. The automated technique, in comparison, was shown to be satisfactory, suggesting the substitution of Timex by Variances imagens, in order to avoid misinterpretation of

the saturated beach. Nevertheless, the search for an optimal shoreline automated detection method was beyond the aim of this work.

To complement the beach evolution study, as well as to give a quick overview of the nourishment works, a nourishment calendar was also developed, where the different nourishment phases and zones were identified. Overall, at each zone, every phase was undertaken at the same time, and each zone was finished usually after one day of works. Still, the sand injection phase on the zones where the two sites where umbrellas are installed for beach users, during the summer months, took two days. The pipe-laying phase, on the northern sector, also lasted longer, as they were already preparing the nourishment works on the next beach.

Concerning the topographic surveys, these allowed for the estimation of the evolution of the sand volume at the beach. Before nourishment, in July, the estimated sand volume was approximately 33 000 m^3, whereas in October, after nourishment, it was over 100 000 m^3. The total volume difference between these months suggests the volume of sand injected into the beach, during the nourishment works, was about 70 000 m^3, instead of the 140 000 m^3 estimated by APA. This major difference could be explained because the volume estimations were calculated by default – not including the entire cross-shore beach extension, as the different profiles surveyed did not cover the same extension and stopped at different elevations.

For the calculated volumes to be closer to the real values, the elevation values could have been extrapolated until the 0 m elevation. By doing this, the comparison between the different estimated sand volumes would have been more accurate and would have allowed for the comparison of the beach profiles with the calculated shorelines for the same period. This approach will be considered in future developments of the present study.

To further improve the study, the $Hs_{b,v24}$ method was tested, in order to estimate the wave height at the study site, using Timex images. Although the measurements were negatively affected by rain drops and dust on the lens, and meteorological factors which lowered the visibility of the beach, and it returned a poor description of the breaking pattern when rip currents were present on the nearshore, the results were satisfactory and an automated algorithm to discard low-quality images will be developed.

The insights gained from this study, regarding the shoreline variability and identification of the beach zones more vulnerable to erosion, could be useful to increase the effectiveness of the yearly nourishment works through time, as well as to help preventing the occurrence of such erosion events in the future, at the study site. However, the analysis was limited to shoreline advance and retreat, not allowing to accurately determine the variation of beach volume, as well as

the longshore sediment transport dynamics. Because of this, further work will increase the beach profile surveys frequency and use a longer video dataset to thoroughly evaluate the efficacy and effectiveness of the nourishment works.

It is expected to fully automatize the coastal video system, which will allow to fully describe the nearshore hydrodynamics and morphology – providing continuous data about the study site, complementing additional monitoring studies. In fact, the automated shoreline detection will be combined with the video-derived breaking wave height, in order to build a video-based integrated system – allowing to study, describe and analyse the nearshore hydrodynamics and morphology, in terms of shoreline, breaking wave height and nearshore bathymetry and hydrodynamics

Furthermore, this study demonstrated the success of using a low-cost video monitoring system to study the coastal morphodynamic evolution. Contrary to more robust video monitoring systems, the data pre- and post- processing must be performed remotely, requiring the collection of the image data from the station. Nonetheless, with the development and automatization of the system, the constraints of data collecting, and treatment will be surpassed. Additionally, despite being a low-cost system, it is widely versatile and resistant to different meteorological events, therefore being a strong and innovative method for coastal morphodynamic monitoring studies in Costa de Caparica.

References

Aarninkhof, S.G.J., Turner, I.L., Dronkers, T.D.T., Caljouw, M., Nipius, L., 2003. A video-based technique for mapping intertidal beach bathymetry. Coastal Engineering 49, 275–289. https://doi.org/10.1016/S0378-3839(03)00064-4

Abessolo Ondoa, G., Almar, R., Kestenare, E., Bahini, A., Houngue, G.-H., Jouanno, J., Du Penhoat, Y., Castelle, B., Melet, A., Meyssignac, B., Anthony, E.J., Laibi, R., Alory, G., Ranasinghe, R., 2016. Potential of Video Cameras in Assessing Event and Seasonal Coastline Behaviour: Grand Popo, Benin (Gulf of Guinea). Journal of Coastal Research 75, 442–446. https://doi.org/10.2112/SI75-089.1

Aedla, R., Dwarakish, G.S., Reddy, D.V., 2015. Automatic Shoreline Detection and Change Detection Analysis of Netravati-GurpurRivermouth Using Histogram Equalization and Adaptive Thresholding Techniques. Aquatic Procedia 4, 563–570. https://doi.org/10.1016/j.aqpro.2015.02.073

Agência Portuguesa do Ambiente, 2019. Alimentação artificial de praias na Costa de Caparica [WWW Document]. URL https://apambiente.pt/ajaxpages/destaque.php?id=1287 (accessed 1.6.20).

Almar, R., Cienfuegos, R., Catalán, P., Birrien, F., Castelle, B., Michallet, H., 2011. Nearshore bathymetric invesion from video using a fully non-linear Boussinesq wave model 64, 3–7.

Andriolo, U., 2019. Nearshore Wave Transformation Domains from Video Imagery. JMSE 7, 186. https://doi.org/10.3390/jmse7060186

Andriolo, U., 2018. Nearshore hydrodynamics and morphology derived from video imagery (PhD thesis). Faculdade de Ciências da Universidade de Lisboa, Lisbon.

Andriolo, U., Almeida, L.P., Almar, R., 2018. Coupling terrestrial LiDAR and video imagery to perform 3D intertidal beach topography. Coastal Engineering 140, 232–239. https://doi.org/10.1016/j.coastaleng.2018.07.009

Andriolo, U., Mendes, D., Taborda, R., 2020. Breaking Wave Height Estimation from Timex Images: Two Methods for Coastal Video Monitoring Systems. Remote Sensing 12, 204. https://doi.org/10.3390/rs12020204

Andriolo, U., Sánchez-García, E., Taborda, R., 2019. Operational use of surfcam online streaming images for coastal morphodynamic studies. Remote Sensing 11. https://doi.org/10.3390/rs11010078

Angnuureng, D.B., 2016. Shoreline response to multi-scale oceanic forcing from video imagery (PhD thesis). Université de Bordeaux, Bordeaux.

Archetti, R., Vacchi, M., Bertoncini, L., Conserva, R., Michela, S., Sigismondi, D., Parlagreco, L., 2014. Coastal monitoring through video systems: best practices and architectural design of a new video monitoring network at Marina di Massa (Tuscany). Coastal erosion monitoring - A network of regional observatories. Results from ResMar Project 157–167.

Archetti, R., Zanuttigh, B., 2010. Integrated monitoring of the hydro-morphodynamics of a beach protected by low crested detached breakwaters. Coastal Engineering 57, 879–891. https://doi.org/10.1016/j.coastaleng.2010.05.002

Baills, A., Garcin, M., Bulteau, T., 2020. Assessment of selected climate change adaptation measures for coastal areas. Ocean & Coastal Management 185, 105059. https://doi.org/10.1016/j.ocecoaman.2019.105059

Boak, E.H., Turner, I.L., 2005. Shoreline Definition and Detection: A Review. Journal of Coastal Research 214, 688–703. https://doi.org/10.2112/03-0071.1

Bouguet, J.-Y., 2015. Camera Calibration Toolbox for Matlab [WWW Document]. URL http://www.vision.caltech.edu/bouguetj/calib_doc/

Bracs, M.A., 2016. Evaluation of Opportunistic Shoreline Monitoring Capability Utilizing Existing "Surfcam" Infrastructure. Journal of Coastal Research 32, 542. https://doi.org/10.2112/JCOASTRES-D-14-00090.1

Brignone, M., Corradi, N., Ferrari, M., Schiaffino, C.F., 2008. Evaluation of a nourishment programme with a webcam: The case of Levanto (La Spezia, Italy). Chemistry and Ecology 24, 207–214. https://doi.org/10.1080/02757540801965407

Brignone, M., Schiaffino, C.F., Isla, F.I., Ferrari, M., 2012. A system for beach video-monitoring: Beachkeeper plus. Computers & Geosciences 49, 53–61. https://doi.org/10.1016/j.cageo.2012.06.008

Brodie, K.L., Bruder, B.L., Slocum, R.K., Spore, N.J., 2019. Simultaneous Mapping of Coastal Topography and Bathymetry From a Lightweight Multicamera UAS. IEEE Trans. Geosci. Remote Sensing 57, 6844–6864. https://doi.org/10.1109/TGRS.2019.2909026

Castelle, B., Turner, I.L., Bertin, X., Tomlinson, R., 2009. Beach nourishments at Coolangatta Bay over the period 1987–2005: Impacts and lessons. Coastal Engineering 56, 940–950. https://doi.org/10.1016/j.coastaleng.2009.05.005

Chang, Jin, Jeong, Kim, Do, 2019. Video Monitoring of Shoreline Positions in Hujeong Beach, Korea. Applied Sciences 9, 4984. https://doi.org/10.3390/app9234984

Chen, W.-W., Chang, H.-K., 2009. Estimation of shoreline position and change from satellite images considering tidal variation. Estuarine, Coastal and Shelf Science 84, 54–60. https://doi.org/10.1016/j.ecss.2009.06.002

Chiva, L., Pagán, J.I., López, I., Tenza-Abril, A.J., Aragonés, L., Sánchez, I., 2018. The effects of sediment used in beach nourishment: Study case El Portet de Moraira beach. Science of The Total Environment 628–629, 64–73. https://doi.org/10.1016/j.scitotenv.2018.02.042

Coelho, C.D.B., 2005. Riscos de Exposição de Frentes Urbanas para Diferentes Intervenções de Defesa Costeira (PhD thesis). Universidade de Aveiro, Aveiro.

Dewi, R.S., Bijker, W., 2019. Dynamics of shoreline changes in the coastal region of Sayung, Indonesia. The Egyptian Journal of Remote Sensing and Space Science S1110982318302722. https://doi.org/10.1016/j.ejrs.2019.09.001

Dodet, G., Bertin, X., Taborda, R., 2010. Wave climate variability in the North-East Atlantic Ocean over the last six decades. Ocean Modelling 31, 120–131. https://doi.org/10.1016/j.ocemod.2009.10.010

Duarte, C.M., Ferreira, J.C., Fortes, J., 2020. Risk Modelling in Urban Coastal Areas to Support Adaptation to Climate Change and Extreme Weather Events: Early Warning, Emergency Planning and Risk Management Systems. Journal of Coastal Research 95, 785. https://doi.org/10.2112/SI95-153.1

Elko, N.A., Holman, R.A., Gelfenbaum, G., 2005. Quantifying the Rapid Evolution of a Nourishment Project with Video Imagery. Journal of Coastal Research 214, 633–645. https://doi.org/10.2112/04-0280.1

Emami, A., Bryan, K.R., Lange, W.P. de, 2019. Spatial Patterns in Groundwater Seepage and Surf Zone Morphology: Muriwai Beach, New Zealand. Journal of Coastal Research 35, 186. https://doi.org/10.2112/JCOASTRES-D-17-00180.1

Ferreira, J.C.R., 2016. Ordenamento Ambiental de Frentes Urbanas Litorais em Áreas Baixas de Elevado Risco e Vulnerabilidade ao Galgamento Costeiro. As Infraestruturas Verdes como Estratégia de Resiliência para as Comunidades Costeiras. (PhD thesis). Universidade Nova de Lisboa, Caparica.

García-Rubio, G., Huntley, D., Russell, P., 2015. Evaluating shoreline identification using optical satellite images. Marine Geology 359, 96–105. https://doi.org/10.1016/j.margeo.2014.11.002

Gargiulo, C., Battarra, R., Tremiterra, M.R., 2020. Coastal areas and climate change: A decision support tool for implementing adaptation measures. Land Use Policy 91, 104413. https://doi.org/10.1016/j.landusepol.2019.104413

Guedes, R.M.C., Calliari, L.J., Holland, K.T., Plant, N.G., Pereira, P.S., Alves, F.N.A., 2011. Short-term sandbar variability based on video imagery: Comparison between Time–Average and Time–Variance techniques. Marine Geology 289, 122–134. https://doi.org/10.1016/j.margeo.2011.09.015

Hagenaars, G., de Vries, S., Luijendijk, A.P., de Boer, W.P., Reniers, A.J.H.M., 2018. On the accuracy of automated shoreline detection derived from satellite imagery: A case study of the sand motor mega-scale nourishment. Coastal Engineering 133, 113–125. https://doi.org/10.1016/j.coastaleng.2017.12.011

Harley, M.D., Andriolo, U., Armaroli, C., Ciavola, P., 2014. Shoreline rotation and response to nourishment of a gravel embayed beach using a low-cost video monitoring technique: San Michele-Sassi Neri, Central Italy. J Coast Conserv 18, 551–565. https://doi.org/10.1007/s11852-013-0292-x

Heikkila, J., Silven, O., 1997. A four-step camera calibration procedure with implicit image correction, in: Proceedings of IEEE Computer Society Conference on Computer Vision and Pattern Recognition. Presented at the IEEE Computer Society Conference on Computer Vision and Pattern Recognition, IEEE Comput. Soc, San Juan, Puerto Rico, pp. 1106–1112. https://doi.org/10.1109/CVPR.1997.609468

Holman, R.A., Stanley, J., 2007. The history and technical capabilities of Argus. Coastal Engineering 54, 477–491. https://doi.org/10.1016/j.coastaleng.2007.01.003

Holthuijsen, L.H., 2007. Waves in oceanic and coastal waters. Cambridge University Press, Cambridge.

Junta de Freguesia Costa de Caparica, 2019. Turismo e Economia [WWW Document]. URL https://www.jf-costacaparica.pt/pt/costa-de-caparica/turismoeconomia.html (accessed 1.6.20).

Karambas, T.V., Samaras, A.G., 2014. Soft shore protection methods: The use of advanced numerical models in the evaluation of beach nourishment. Ocean Engineering 92, 129–136. https://doi.org/10.1016/j.oceaneng.2014.09.043

Karasu, S., Work, P.A., Uzlu, E., Kankal, M., Yüksek, Ö., 2016. Beach nourishment alternative assessment to constrain cross-shore and longshore sediment transport. Applied Ocean Research 59, 459–471. https://doi.org/10.1016/j.apor.2016.07.001

Kermani, S., Boutiba, M., Guendouz, M., Guettouche, M.S., Khelfani, D., 2016. Detection and analysis of shoreline changes using geospatial tools and automatic computation: Case of jijelian sandy coast (East Algeria). Ocean & Coastal Management 132, 46–58. https://doi.org/10.1016/j.ocecoaman.2016.08.010

Kroon, A., Davidson, M.A., Aarninkhof, S.G.J., Archetti, R., Armaroli, C., Gonzalez, M., Medri, S., Osorio, A., Aagaard, T., Holman, R.A., Spanhoff, R., 2007. Application of remote sensing video systems to coastline management problems. Coastal Engineering 54, 493–505.

Ludka, B.C., Guza, R.T., O'Reilly, W.C., 2018. Nourishment evolution and impacts at four southern California beaches: A sand volume analysis. Coastal Engineering 136, 96–105. https://doi.org/10.1016/j.coastaleng.2018.02.003

Luo, S., Liu, Y., Jin, R., Zhang, J., Wei, W., 2016. A guide to coastal management: Benefits and lessons learned of beach nourishment practices in China over the past two decades. Ocean & Coastal Management 134, 207–215. https://doi.org/10.1016/j.ocecoaman.2016.10.011

Mahabot, M.-M., Jaud, M., Pennober, G., Le Dantec, N., Troadec, R., Suanez, S., Delacourt, C., 2017. The basics for a permanent observatory of shoreline evolution in tropical environments; lessons from back-reef beaches in La Reunion Island. Comptes Rendus Geoscience 349, 330–340. https://doi.org/10.1016/j.crte.2017.09.010

Marinho, B., Coelho, C., Hanson, H., Tussupova, K., 2019. Coastal management in Portugal: Practices for reflection and learning. Ocean & Coastal Management 181, 104874. https://doi.org/10.1016/j.ocecoaman.2019.104874

Matias, A., Rita Carrasco, A., Loureiro, C., Masselink, G., Andriolo, U., McCall, R., Ferreira, Ó., Plomaritis, T.A., Pacheco, A., Guerreiro, M., 2019. Field measurements and hydrodynamic modelling to evaluate the importance of factors controlling overwash. Coastal Engineering 152, 103523. https://doi.org/10.1016/j.coastaleng.2019.103523

Ojeda, E., Guillén, J., 2006. Monitoring beach nourishment based on detailed observations with video measurements. Journal of Coastal Research 7.

Osorio, A.F., Medina, R., Gonzalez, M., 2012. An algorithm for the measurement of shoreline and intertidal beach profiles using video imagery: PSDM. Computers & Geosciences 46, 196–207. https://doi.org/10.1016/j.cageo.2011.12.008

Pearre, N.S., Puleo, J.A., 2009. Quantifying Seasonal Shoreline Variability at Rehoboth Beach, Delaware, Using Automated Imaging Techniques. Journal of Coastal Research 254, 900–914. https://doi.org/10.2112/08-1029.1

Pereira, P.S., Calliari, L.J., Holman, R., Holland, K.T., Guedes, R.M.C., Amorin, C.K., Cavalcanti, P.G., 2011. Video and field observations of wave attenuation in a muddy surf zone. Marine Geology 279, 210–221. https://doi.org/10.1016/j.margeo.2010.11.004

Pianca, C., Holman, R., Siegle, E., 2015. Shoreline variability from days to decades: Results of long-term video imaging. J. Geophys. Res. Oceans 120, 2159–2178. https://doi.org/10.1002/2014JC010329

Pinto, C.A., Silveira, T.M., Teixeira, S.B., 2018. Alimentação Artificial de Praias na faixa costeira de Portugal Continental: Enquadramento e Restrospetiva das intervenções realizadas (1950-2017). Agência Portuguesa do Ambiente.

Plant, N.G., Holman, R.A., 1997. Intertidal beach profile estimation using video images. Marine Geology 140, 1–24. https://doi.org/10.1016/S0025-3227(97)00019-4

Ponte Lira, C., Nobre Silva, A., Taborda, R., Freire de Andrade, C., 2016. Coastline evolution of Portuguese low-lying sandy coast in the last 50 years: an integrated approach. Earth Syst. Sci. Data 8, 265–278. https://doi.org/10.5194/essd-8-265-2016

Pugliano, G., Robustelli, U., Di Luccio, D., Mucerino, L., Benassai, G., Montella, R., 2019. Statistical Deviations in Shoreline Detection Obtained with Direct and Remote Observations. JMSE 7, 137. https://doi.org/10.3390/jmse7050137

Rigos, A., Tsekouras, G.E., Vousdoukas, M.I., Chatzipavlis, A., Velegrakis, A.F., 2016. A Chebyshev polynomial radial basis function neural network for automated shoreline extraction from coastal imagery. ICA 23, 141–160. https://doi.org/10.3233/ICA-150507

Sánchez-García, E., Balaguer-Beser, A., Pardo-Pascual, J.E., 2017. C-Pro: A coastal projector monitoring system using terrestrial photogrammetry with a geometric horizon constraint. ISPRS Journal of Photogrammetry and Remote Sensing 128, 255–273. https://doi.org/10.1016/j.isprsjprs.2017.03.023

Semeoshenkova, V., Newton, A., 2015. Overview of erosion and beach quality issues in three Southern European countries: Portugal, Spain and Italy. Ocean & Coastal Management 118, 12–21. https://doi.org/10.1016/j.ocecoaman.2015.08.013

Senechal, N., Coco, G., Bryan, K.R., Holman, R.A., 2011. Wave runup during extreme storm conditions. J. Geophys. Res. 116, C07032. https://doi.org/10.1029/2010JC006819

Silva, A.N., 2014. Beach Morphodynamics at Nazaré coast using video monitoring (PhD thesis). Faculdade de Ciências da Universidade de Lisboa, Lisboa.

Silva, S.F., Martinho, M., Capitão, R., Reis, T., Fortes, C.J., Ferreira, J.C., 2017. An index-based method for coastal-flood risk assessment in low-lying areas (Costa de Caparica, Portugal). Ocean & Coastal Management 144, 90–104. https://doi.org/10.1016/j.ocecoaman.2017.04.010

Simarro, G., Bryan, K.R., Guedes, R.M.C., Sancho, A., Guillen, J., Coco, G., 2015. On the use of variance images for runup and shoreline detection. Coastal Engineering 99, 136–147. https://doi.org/10.1016/j.coastaleng.2015.03.002

Splinter, K., Harley, M., Turner, I., 2018. Remote Sensing Is Changing Our View of the Coast: Insights from 40 Years of Monitoring at Narrabeen-Collaroy, Australia. Remote Sensing 10, 1744. https://doi.org/10.3390/rs10111744

Splinter, K.D., Strauss, D.R., Tomlinson, R.B., 2011. Assessment of Post-Storm Recovery of Beaches Using Video Imaging Techniques: A Case Study at Gold Coast, Australia. IEEE Trans. Geosci. Remote Sensing 49, 4704–4716. https://doi.org/10.1109/TGRS.2011.2136351

Taborda, R., Silva, A., 2012. COSMOS: A lightweight coastal video monitoring system. Computers & Geosciences 49, 248–255. https://doi.org/10.1016/j.cageo.2012.07.013

Thuan, D.H., Almar, R., Marchesiello, P., Viet, N.T., 2019. Video Sensing of Nearshore Bathymetry Evolution with Error Estimate. JMSE 7, 233. https://doi.org/10.3390/jmse7070233

Thurman, H.V., Trujillo, A.P., 1999. Essentials of oceanography, 6. ed. ed. Prentice Hall, Upper Saddle River, NJ.

Uunk, L., Wijnberg, K.M., Morelissen, R., 2010. Automated mapping of the intertidal beach bathymetry from video images. Coastal Engineering 57, 461–469. https://doi.org/10.1016/j.coastaleng.2009.12.002

Valentini, N., Saponieri, A., Damiani, L., 2017a. A new video monitoring system in support of Coastal Zone Management at Apulia Region, Italy. Ocean & Coastal Management 142, 122–135. https://doi.org/10.1016/j.ocecoaman.2017.03.032

Valentini, N., Saponieri, A., Molfetta, M.G., Damiani, L., 2017b. New algorithms for shoreline monitoring from coastal video systems. Earth Sci Inform 10, 495–506. https://doi.org/10.1007/s12145-017-0302-x

Veloso-Gomes, F., Costa, J., Rodrigues, A., Taveira-Pinto, F., Pais-Barbosa, J., Neves, L., 2009. Costa da Caparica Artificial Sand Nourishment and Coastal Dynamics. Journal of Coastal Research 56, 678–682.

Vos, K., Harley, M.D., Splinter, K.D., Simmons, J.A., Turner, I.L., 2019a. Sub-annual to multi-decadal shoreline variability from publicly available satellite imagery. Coastal Engineering 150, 160–174. https://doi.org/10.1016/j.coastaleng.2019.04.004

Vos, K., Splinter, K.D., Harley, M.D., Simmons, J.A., Turner, I.L., 2019b. CoastSat: A Google Earth Engine-enabled Python toolkit to extract shorelines from publicly available satellite imagery. Environmental Modelling & Software 122, 104528. https://doi.org/10.1016/j.envsoft.2019.104528

Vousdoukas, M.I., Almeida, L.P.M., Ferreira, Ó., 2012. Beach erosion and recovery during consecutive storms at a steep-sloping, meso-tidal beach: BEACH EROSION/RECOVERY DURING CONSECUTIVE STORMS. Earth Surf. Process. Landforms 37, 583–593. https://doi.org/10.1002/esp.2264

Vousdoukas, M.I., Ferreira, P.M., Almeida, L.P., Dodet, G., Psaros, F., Andriolo, U., Taborda, R., Silva, A.N., Ruano, A., Ferreira, Ó.M., 2011. Performance of intertidal topography video monitoring of a meso-tidal reflective beach in South Portugal. Ocean Dynamics 61, 1521–1540. https://doi.org/10.1007/s10236-011-0440-5

Annexes

Annex I: Certificate of acceptance of the manuscript

water

an Open Access Journal by MDPI

Indexed in: Ei Compendex

CITESCORE 2.66 SCOPUS

IMPACT FACTOR 2.524

CERTIFICATE OF ACCEPTANCE

Certificate of acceptance for the manuscript (**water-825832**) titled:

Shoreline response to a sandy nourishment in a wave-dominated coast using video monitoring

Authored by:

Catarina Jóia Santos; Umberto Andriolo; José C. Ferreira

has been accepted in *Water* (ISSN 2073-4441) on 04 June 2020

MDPI Academic Open Access Publishing since 1996

Basel, June 2020

Annex II: Shoreline Response to a Sandy Nourishment in a Wave Dominated Coast using Video Monitoring

In this chapter, the formatting characteristics of the *Water* scientific journal have already been applied to the manuscript, resulting in the article displayed below[1].

[1] Jóia Santos, C.; Andriolo, U.; Ferreira, J.C, 2020. Shoreline Response to a Sandy Nourishment in a Wave-Dominated Coast Using Video Monitoring. Water 2020, 12, 1632.
https://doi.org/10.3390/w12061632

water

MDPI

Article

Shoreline Response to a Sandy Nourishment in a Wave-Dominated Coast Using Video Monitoring

Catarina Jóia Santos [1,*], Umberto Andriolo [2] and José C. Ferreira [1]

[1] Department of Environmental Sciences and Engineering, NOVA School of Science and Technology, NOVA University Lisbon/MARE-Marine and Environmental Sciences, Campus da Caparica, 2829-516 Caparica, Portugal; jcrf@fct.unl.pt

[2] Department of Electrical and Computer Engineering, INESC Coimbra, Rua Silvio Lima, Polo II, 3030-290 Coimbra, Portugal; uandriolo@mat.uc.pt

* Correspondence: csj.santos@campus.fct.unl.pt

Received: 20 May 2020; Accepted: 4 June 2020; Published: 6 June 2020

check for updates

Abstract: Beach nourishment is a soft engineering intervention that supplies sand to the shore, to increase the beach recreational area and to decrease coastal vulnerability to erosion. This study presents the preliminary evaluation of nourishment works performed at the high-energy wave-dominated Portuguese coast. The shoreline was adopted as a proxy to study beach evolution in response to nourishment and to wave forcing. To achieve this aim, images collected by a video monitoring system were used. A nourishment calendar was drawn up based on video screening, highlighting the different zones and phases where the works took place. Over the six-month monitoring period, a total amount of 25 video-derived shorelines were detected by both manual and automated procedures on video imagery. Nourishment works, realized in summer, enlarged the emerged beach extension by about 90 m on average. During winter, the shoreline retreated about 50 m due to wave forcing. Spatial analysis showed that the northern beach sector was more vulnerable and subject to erosion, as it is the downdrift side of the groin.

Keywords: beach; nearshore; remote sensing; erosion; sand

1. Introduction

Beach nourishment is a soft engineering intervention that consists of the injection and placement of sediments into the beach system, to extend, widen and elevate the subaerial beach [1–3]. The sediments added to the beach reduce the vulnerability to storms and enhance the wave energy dissipation [4]. Additionally, beach nourishment increases the recreational beach area, leading to positive consequences in tourism [5,6]. In order to evaluate the effectiveness of nourishment works, it is essential to monitor the beach evolution in response to the intervention [6–8].

The shoreline, defined as the dynamic interface between land and ocean, is the most common monitoring coastal indicator in morphodynamic studies [9–11]. As the shoreline constantly changes due to cross-shore and alongshore sediment movement in the littoral zone, as well as because of the dynamic nature of water levels, it reveals helpful information on beach variation, being useful for coastal zone monitoring after nourishment interventions [12–15].

Over the last three decades, shoreline evolution has mostly been studied by remote sensing techniques, namely satellite and shore-based video stations. Satellite imaging is a suitable tool for updating shoreline maps, since they provide long-term observations of coastline changes on regional and national scales [16–21]. Nevertheless, shoreline from satellite can be retrieved with low time frequency, and tidal information at the time of image acquisition is often missing.

In contrast with satellite images, coastal video monitoring provides high-frequency, high-quality and continuous images of the nearshore area [22,23]. Shore-based video systems are composed by optical devices installed on an elevated position observing the nearshore area. The continuous acquisition of images allows the observation of the dynamic changes of the nearshore, including the shoreline, in order to build a long-term dataset for a detailed description of coastal morphodynamic evolution [22–24].

Coastal video monitoring operates specific optical products: Timex and Variance images. Timex are digitally averaged images, collected over a period of sampling (generally 10 min), which smooth out the moving features [25–27]. Variance images are built instead as the standard deviation of the sampled period, showing with bright pixels the areas with larger temporal variability, and with dark pixels the unvaried areas [27–29].

Due to their properties, Timex and Variance images have been widely used to detect the shoreline, as they smooth the water movement on the beach face [12,30–41]. However, he number of video imagery applications to monitor coastal nourishment is scarce [42–45]. Harley et al. [43] analyzed shoreline evolution in response to a gravel beach nourishment on the Adriatic Italian coast, with a focus on coastline rotation and recession in response to storm events. Brignone et al. [45] aimed to test the feasibility of a webcam to evaluate the efficiency of a nourishment project carried out on a gravel beach at the Tyrrhenian coast (Italy). Ojeda and Guillén [44] studied the sandy nourishment in two artificially embayed beaches on the Spanish Mediterranean coast, while Elko et al. [42] applied video imagery to monitor nourishment evolution southern an inlet split in the west coast of Florida, facing the Gulf of Mexico. All these works quantified the effectiveness of nourishment works in extending the beach area, however they were conducted at low-energy and micro-tidal systems, where storms play a major role in shaping the coastline.

The main objective of this work was to monitor the nourishment works and to analyze the preliminary shoreline response on Tarquínio-Paraiso beach, a sandy shore in the high-energy meso-tidal Portuguese Atlantic coast. A shore-based video monitoring station was installed on a hotel roof-top and has been storing high-resolution images of the study site. The collected videos during the nourishment works were visually screened to draw up the nourishment calendar, spatially and temporally locating the three phases of works. The rectified Timex and Variance images were used to detect the shoreline manually and automatically, respectively, over the monitored period of six months. The built shoreline dataset was analyzed to quantify the evolution of the emerged beach extent in response to nourishment, completed in summer, and further to winter high-energy events.

This study constitutes the first analysis of shoreline variation at the study site. Moreover, the automated shoreline detection and a video-derived breaking wave height technique were tested to set the ground for an automated video-based integrated system capable of describing hydro-and morphodynamics of the Tarquínio-Paraíso beach.

2. Methods

2.1. Study Site and Video Station

Costa de Caparica is a sandy stretch located on the south margin of the Tagus river estuary, on the central Portuguese coast (Figure 1a). This area represents the main site for coastal recreational activities of the Lisbon and Setúbal regions [46]. The area has experienced coastline retreat of about 200 m in the last 50 years, resulting in more vulnerability of the urban front to severe storm events [47–49]. In order to protect the urban front, nourishment operations have been performed at Costa de Caparica on an yearly base since 2016 [46]. In 2019, the nourishment activities took place between the 13 August and 24 September. A total sand volume of 1,000,000 m^3 was distributed on the seven beaches of Costa de Caparica, between the northernmost São João beach and the southernmost Nova Praia beach [46].

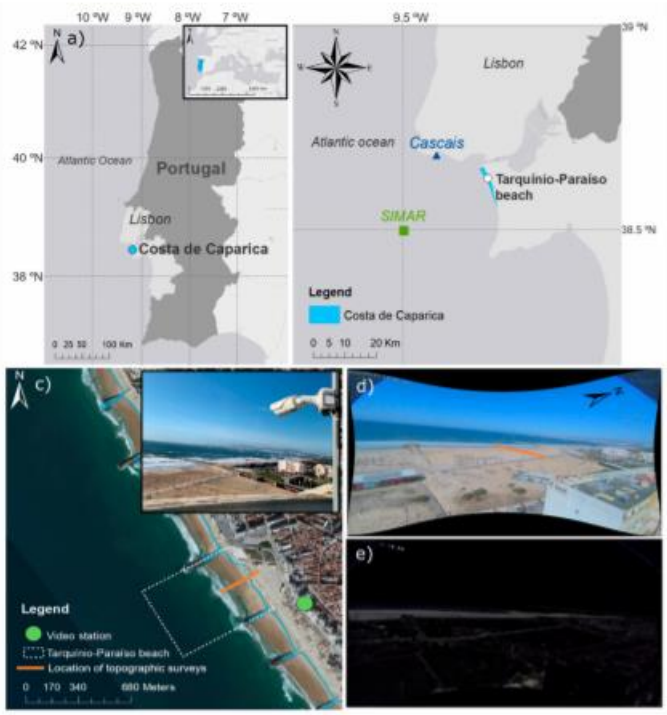

Figure 1. Study site map. (**a**) Location of Costa de Caparica; (**b**) location of Tarquínio-Paraíso beach (circle), Cascais tide gauge (triangle), and SIMAR point (square); (**c**) location of the video-station (in green) and of the cross-shore profile surveyed over the monitored period (orange, see Section 3.2); (**d**) Timex image and (**e**) Variance image.

The study site is the Tarquínio-Paraíso beach (38°38′30.3″ N, 9°14′20.5″ W), the fourth urban beach in Costa de Caparica (Figure 1). The beach extends for about 390 m along the shore with NW-SE orientation, and it is limited sideways by two groins, and landward by a beach wall. The site is characterized by a mesotidal tidal regime, where the average tide amplitude is 2.10 m, and its maximum elevation is 4 m. The wave regime has an average significant height of 2 m, and periods between 7 and 15 s, predominantly coming from Northwest [27,50]. The nourishment activities occurred between 26 August and 4 September 2019, with about 140,000 m^3 of sand placed on the shore [46]. The grain size of the nourished sand (D_{50} = 0.55 mm) matched the characteristics of the native sand [46].

To characterize the topographic changes, a cross-shore beach profile was surveyed with RTK-GPS instrumentation prior and after the nourishment works over six months (Figure 1c,d).

Tidal data was obtained by the tide gauge of Cascais (38.69° N, 9.42° W) (ftp://ftp.dgterritorio.pt/Maregrafos/Cascais_radar/2019/), while Hindcast wave and wind hourly data were provided by Puertos del Estado (http://www.puertos.es), a state-owned Spanish company with headquarters in Spain, at the most representative SIMAR point (38.50° N, 9.50° N) (Figure 1b).

A video-monitoring system, comprising an Internet Protocol Vivotek IB9365-HT camera, was installed on a hotel rooftop at 90 m above mean sea level (MSL), looking at the Tarquínio-Paraíso beach, on 30 July 2019 (Figure 1c). The system has been acquiring video-images at 2 Hz, continuously during daylight hours, recording 15 h per day. In this work, the dataset consisted of 126 days, as video data was lost between 14 November 2019 and 10 January 2020.

The video imagery dataset was corrected by the lens-inducted distortions following the Bouguet procedure [51]. Subsequently, 10-min Timex (Figure 1d) and Variance (Figure 1e) images were produced and rectified at the tidal level corresponding to the acquisition time. The rectification procedure was based on collinearity equations [52,53].

2.2. Beach Nourishment Monitoring

The nourishment works started dredging sand from the bottom of the southern bar channel of the Lisbon port, at about a 17 m depth.

The dredged sand was transported through submerged metal pipes from the drag suction dredge to the shore, where it was pumped on the subaerial beach and repositioned by caterpillars. This nourishment procedure was considered as the most efficient way to avoid the disturbance of fishing boats in the nearshore, and to reduce the environmental impact on the beach [46].

From the collected videos, three main nourishment phases were distinguished (Figure 2):

1. The pipe-laying phase, when tubes coming from the dredge boat to the shore were placed (and moved) on the beach;
2. The sand injection phase, which consisted in the actual nourishment, when the sand was pumped on the beach;
3. The re-distribution phase, when caterpillars redistributed the dredged sand on the beach.

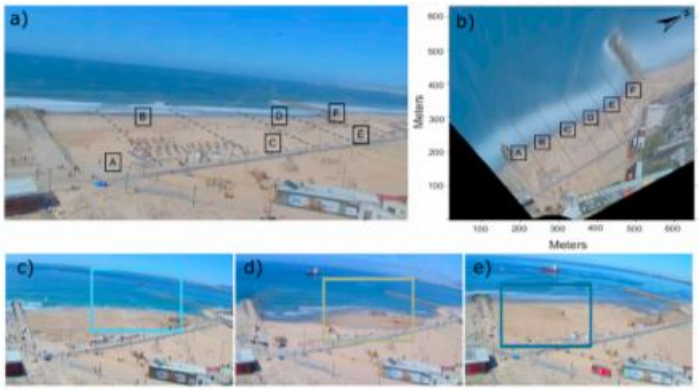

Figure 2. Different nourishment zones and nourishment phases at the Tarquínio-Paraíso beach. (**a**) Nourishment zones; (**b**) nourishment zones displayed on rectified image; (**c**) pipe-laying phase; (**d**) sand injection phase; and (**e**) re-distribution phase. The different rectangles indicate the specific area at the beach where each phase is taking place.

Based on the aforementioned definitions, it was possible to elaborate the nourishment map/calendar, identifying the days and zones where the distinct nourishment phases took place. For a regular elaboration, the beach was divided in six different sectors (Figure 2a,b), each representing an approximate longshore extent of 70 m

2.3. *Shoreline Detection*

In order to describe the shoreline variation over the monitored period, a series of images was selected to apply manual and automated shoreline detection. Considering the video dataset, a first screening excluded poor quality images deteriorated by dust or rain drops on the lens, and those images acquired during adverse weather conditions or affected by sun glitter. A second criterion was to reject images with a crowded beach, as the presence of people on the shore may affect shoreline detection. Finally, among the remaining available video data, images with tidal level corresponding to the MSL were selected (i.e., tidal level within ± 0.02 m), following the procedure proposed by Chang et al. [54] and Harley et al. [43]. This approach allowed to minimize the influence of tidal variability on the resulting shoreline position, and to compare shoreline positions taken at the same sea level.

2.3.1. Manual Shoreline Detection

The manual shoreline detection procedure was performed on rectified Timex in Matlab environment. To make the procedure regular, a series of 37 parallel transects, with an offset of about 10 m and perpendicular to the beach wall, were superimposed on the image (Figure 3). The detection process consisted in manually marking the limit between water and dry sand at each transect, interpreted as such by the operator.

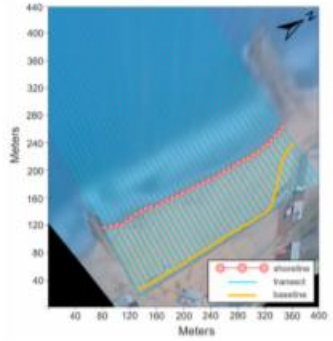

Figure 3. Manual shoreline detection procedure performed in Matlab environment. The red circles indicate the point where each transect intercepts the limit between water and dry sand, and the whole set of 37 points represent the shoreline position. The yellow line indicates the baseline, which corresponds to the position of the beach wall, against which the shoreline position is measured.

The baseline chosen corresponded to the beach wall backing the beach. Therefore, the actual cross-shore extent of the emerged beach was found by subtracting the baseline, at each transect, from the shoreline position. The shoreline variation analysis consisted in comparing the shorelines detected over the monitored period.

2.3.2. Automated Shoreline Detection

Besides manual detection, a dedicated algorithm was implemented to automatically mark the shoreline. For the automated detection, Variance images were chosen as principal sources, and the same 37 transects used for the manual detection were exploited for sampling pixel intensity.

Given I_{TX} the pixel intensity sampled on Timex, and I_{VAR} the pixel intensity sampled on Variance on the transects (see Andriolo et al. [27] for a detailed explanation), the steps undertaken by the Matlab-based detection algorithm were the following:

1. Masking dry beach. The color ratio Red: Green bands were computed from I_{TX} profile. A conservative value of 1.4 was used to filter out the emerged beach on I_{VAR}, similar to the method in Andriolo et al. [27].
2. Min–Max normalization of the Blue band of I_{VAR}. The pixel intensity statistical values of I_{VAR} are transformed to the range 0–1.
3. Smoothing data. I_{VAR} are smoothed with a moving average window of 10% of the total transect length.
4. Masking surf zone. We searched the first peak of I_{VAR} seaward the dry beach limit, which identifies the surf–swash zone boundary (Sw_{min}, as proven in Andriolo et al. [27]).
5. Detrending. The mean value of I_{VAR} profile, taken between the dry beach and the swash zone limits, is subtracted from the main vector.
6. Shoreline detection. The shoreline is identified at the cross-shore location in which I_{VAR} has a null value.

3. Results

3.1. Hydrodynamics

Figure 4 shows the hydrodynamics during the monitored period. The highest H_s values and the most energetic days occurred between November and January, the main event being in December with the maximum H_s = 7 m. The wave direction varied between 225° and 350°, with predominant Northwest (NW) direction.

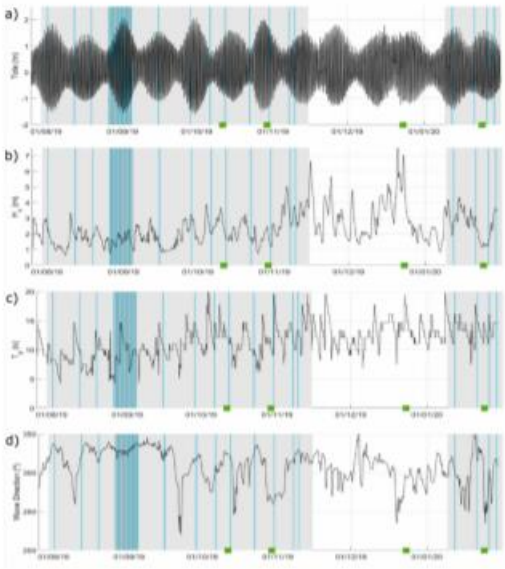

Figure 4. Hydrodynamics of the study site. (**a**) Tide level from Cascais tide gauge; (**b**) significant wave height; (**c**) wave period; and (**d**) wave direction (from Puertos del Estado). Light gray rectangles indicate the video-monitoring period, blue vertical lines indicate the days chosen for shoreline detection, and the green squares represent the days topographic surveys were performed during the monitored period.

Figure 4 also indicates the days chosen for shoreline detection and the days where beach profile surveys were performed. Over the monitored period, the shoreline detection frequency was biweekly. Nonetheless, during the nourishment period, the shoreline was detected daily to describe the evolution of the beach extent. Moreover, in November and January, the shoreline was detected weekly, as high energy episodes were more frequent. The topographic surveys represented were performed after the nourishment works over the monitored period to quantify the 3D evolution of the beach profile.

3.2. Beach Profile Evolution

Figure 5 shows the topographic evolution of the chosen beach profile (see Figure 1c,d for location on the beach). The profile of 18 July 2019 corresponded to the beach configuration prior to the nourishment and the monitoring period (slope of 0.035), while the profiles acquired in October were the first-available beach configuration after the nourishment.

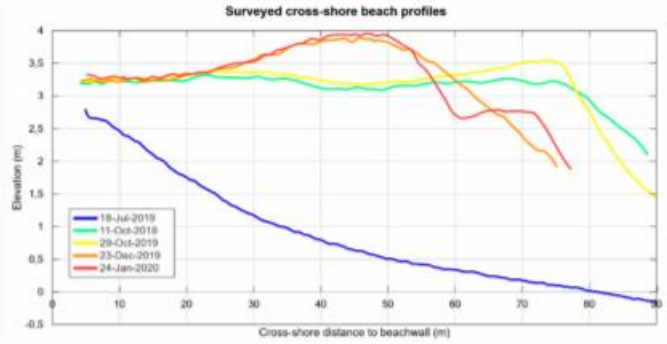

Figure 5. Surveyed cross-shore beach profiles of the Tarquínio-Paraíso beach. The elevation of each profile is referred to mean sea level (MSL).

At 60 m location, the slope was inferior to 0.01, showing little variation in elevation between the surveys. After 60 m, the profile from 29 October showed an increase in elevation of about 0.30 m, when compared with the previous profile, which could be attributed to the deposition of sediments by strong waves registered between 27 and 29 October 2019.

The profile of December showed a dome of sand accumulation of 1 m between the 25 and 60 m locations. There was an increase in the frictional forces between the high energy waves, because of the high energy episodes in December (Figure 4b) and the beach surface, resulting in more sediment deposition in this area. This dome represented an increase of approximately 27 m^2/m in sand volume, in comparison with October, for that same area. Moreover, on the January profile, while there were no high energy events comparable with the ones from December, according to Figure 4b and the available video data, the sediment accumulation dome prevailed. After December, some of the accumulated sediments started being mobilized by wave action, resulting in a secondary berm, at 60 m location.

Considering the surveyed cross-sections (Figure 5), the unit beach volumes were estimated as the volume of sand contained in a unit length of beach, computing the integral of the beach profiles. Before nourishment, the unit volume was about 83 m^2/m, and increased to 263 m^2/m after the nourishment works. By the end of the monitored period, in January, the unit volume decreased to 235 m^2/m. The estimation of the total volume of the beach accounted for the longshore extension of 390 m. The total sand volume was approximately 33,000 m^3 prior to the nourishment, over 100,000 m^3 in October, and about 90,000 m^3 in January.

3.3. *Beach Nourishment*

Nourishment Calendar

The nourishment calendar is shown on Figure 6. The nourishment activities started from the central zone of the beach (zones B and C), and then moved to zones A and D. Finally, on the last days of the nourishment period, the works took place on zones E and F, located on the northern sector of the beach.

Figure 6. The beach nourishment works calendar for the nourishment period. (**a**) Nourishment zones; (**b**) nourishment zones displayed on rectified image; (**c**) the nourishment calendar, indicating the zones where each phase took place, on each day.

The three phases were conducted and completed in each sector (or sectors, if they were being conducted on different zones, at the same time), before moving to the next one. On each different zone, the works were completed in 1–2 days, the exception being zone F. On the last two days of nourishment, the sand injection and re-distribution phases had already ceased, only the pipe-laying phase was still occurring on zone F, as they were already preparing the tubes for the nourishment works on the next beach.

3.4. *Shoreline Variability*

The shoreline variation registered over the monitored period is shown in Figure 7. The initial emerged beach extension was inferior to 50 m. After the nourishment works, the shoreline advanced between 80 and 100 m, for the entire longshore extension, resulting in an emerged beach width of 130 m on average. Between November and January, due to high energy wave events, the shoreline retreated over 30 m. It was not possible, however, to analyze the shoreline position evolution during this phase since it coincided with the data loss period. On the last monitored days, the emerged beach width was about 30 m larger than in August, on average.

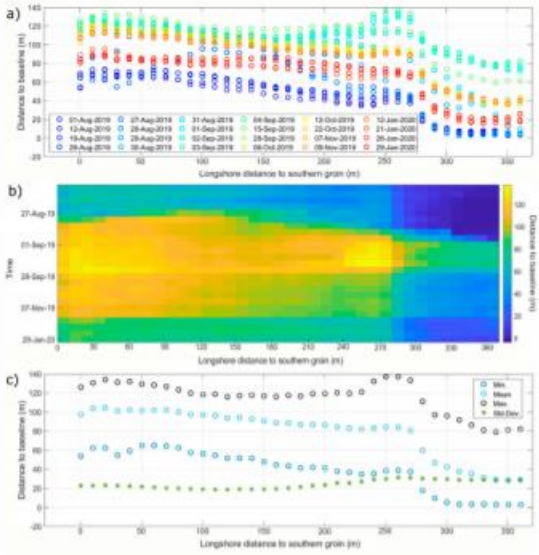

Figure 7. Shoreline position evolution. (**a**) Shoreline evolution through the monitoring period (August–January); (**b**) time-space image displaying the shoreline evolution: rows indicate the date of Timex used for the shoreline detection, columns represent the longshore distance (space) from the southern limit of the beach, color represents the beach width; (**c**) the minimum, mean, maximum, and standard deviation values of distance to baseline/beach extension, during the monitored period.

In general, the southern sector of the beach registered the largest emerged beach width, while the northern sector was the area most affected by erosion events, with significant shorter mean beach extent (Figure 7c). The standard deviation values reached its peak around 250 m from the southern groin (Figure 7c), as supported by the significant increase in beach width registered for that same area, during the nourishment (Figure 7b).

Manual vs. Automated Shoreline Detection

The relation between manual and automated shoreline detection is shown on Figure 8. The automated results were satisfactory, with a median disparity of 5 m and an averaged RMSE of 10 m, when compared with the manual technique. Considering the transects, the southern sector was more difficult to retrieve automatically in comparison with the northern sector. This may be due to the lower resolution of the rectified images on the southern sector since it was the furthest from the camera. The detection on the northern limit profiles was also affected by some uncertainties, perhaps due to the sampled transects being closer to the groin on rectified images. Here, the sampling algorithm may have been affected by shadow and wave diffraction generated by the groin. Considering the automated shorelines detected over time, it is of interest to note that later shorelines (November 2019 and January 2020) were detected slightly seaward when compared to the manual shorelines (about 5 m on average). During more energetic days, it was more difficult to visually identify the limit between water and dry sand on Timex, as swash excursion was larger and more irregular. In this regard, Variance images are more appropriate to correctly identify the averaged swash.

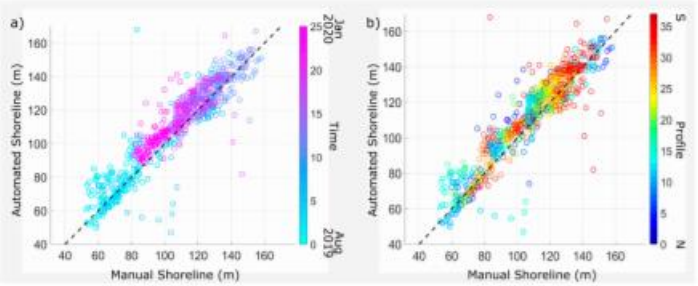

Figure 8. Manual and automated shoreline detection. (**a**) Comparison based on shoreline date; (**b**) comparison based on sampled transect. Dashed black line indicates identity.

4. Discussion

In this work, the shore-based video imagery technique confirmed its versatility and suitability to monitor nourishment works and study coastal processes. The beach nourishment calendar (Section 3.3) provided a spatial and temporal overview of the procedures, by identifying the different zones and phases of the nourishment works. The example shown in Figure 6 was useful to understand the nourishment dynamics and provides a useful costal management tool for supervising the works on the beach. It is worth noting that in the works monitored by Harley et al. [43] on the low-energy Adriatic coast, the sediment (mixed gravel) was deposited by the dredger directly on the shore and redistributed by wave action. Since the dredger needed to repeat the action of digging, transporting and releasing the material several times, nourishment works lasted about 22 days for an embayed beach of 1 km. In this study case, the sand was transported through pipes from the dredgers to the shore and reallocated by caterpillars on the emerged beach. Although the use of machineries may have a negative ecological impact on the beach, this allowed us to fasten the works and complete the nourishment of the Tarquínio-Paraíso beach (390 m) in about one week.

The use of continuous video monitoring allowed the detailed quantification of the success of the nourishment project in increasing the width and area of the emerged beach (Section 3.4). However, the analysis was limited to shoreline advance and retreat, as video imagery did not permit the evaluation of the variation of beach volume. It was not possible to distinguish the influence of longshore and cross-shore transports in sediment dynamics. On one hand, the beach orientation (NW-SE) in relation to the predominant wave direction (NW) indicate that longshore current may have a significant impact in shaping the beach, in particular in the downdrift side of northern groin. On the other hand, the limited length of the beach (390 m) suggests that cross-shore sediment transport may play the major role in beach erosion and accretion. Similar constraints related to shoreline-based studies were highlighted by the other authors that used video monitoring technique to evaluate nourishment works [43,44], although these analysis regarded shoreline variation at low-energy Adriatic and Mediterranean coast.

The beach profile analysis (Figure 5) has shown that sand was moved up the intertidal area by storms during the energetic winter months, when shoreline analysis indicated shoreline retreat of about 30 m in respect to autumn months. The sand on the emerged beach has likely remained in the beach system though, as coastal processes likely redistributed the sand on the shore and perhaps increasing the dry beach area. In this regard, further work will increase the frequency of beach profile surveys and use a longer video dataset to fully evaluate the efficacy and effectiveness of the nourishment performed in summer 2019.

The coastal video station has been installed with the aim of a long-term monitoring of the coastal evolution of the Tarquínio-Paraíso beach, and it is still operative. In this perspective, the automated shoreline detection proposed in this work (Section 3.4), similar to Emami et al. [55], was shown to

be reliable and returned adequate resolution when compared to the manual detection. At the study site, the use of Variance images for developing the automated algorithm was chosen, as the saturated beach may affect and mislead the shoreline detection on Timex [30,33,37,56,57]. Automated detection also overcomes the subjectivity of manual procedure, since the identification of the water–sand limit is based on the operator interpretation. Nevertheless, the use of Variance is recommended for detecting the shoreline on an unoccupied beach. The presence of people (beachgoers, fishermen, surfers etc.) and moving objects (tractors, quads etc.) are highlighted on Variance as bright pixels like the swash movement exploited to detect the shoreline. Therefore, a crowded beach negatively affects the automated detection [27], whereas on Timex moving effects are smoothed out [22,23].

To improve the morphodynamic analysis, the $Hs_{b,r24}$ method [58] was tested, to estimate the wave height using Timex image (Figure 9). The method is based on the findings that the cross-shore length of the typical time-averaged signature of breaking wave foam on Timex, can be empirically associated with the local water depth at breaking, thus to breaking wave height [58].

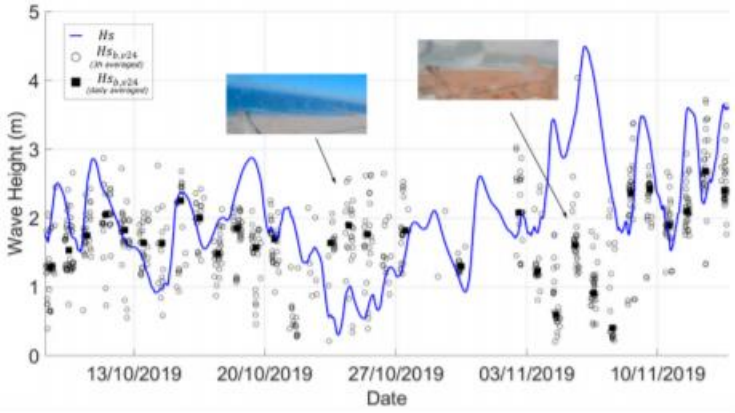

Figure 9. Video-derived breaking wave height $Hs_{b,r24}$ [58]. Insets show two examples of images with dirty lens, rain drops and presence of rip currents in the nearshore, which led to poor results.

A total amount of 35 days, covered by about 3000 rectified Timex images, were processed to sample the wave breaking bright pixel pattern over the nearshore bar and eventually applying $Hs_{b,r24}$ method to retrieve the estimation of breaking wave height for each 10-min Timex. The video-derived results were 3-h and daily averaged to be compared to 3-h offshore wave data available (Section 3.1). Overall, the video-derived wave height had a correlation coefficient of 0.35 with the offshore data. Although the propagation of offshore data, considering period and direction, would have provided a more reliable evaluation of video-results, at this stage it was not considered. The measures were negatively affected by rain drops and dust on the lens, presence of mist and low visibility on the beach (Figure 9). In addition, the fully automated methodology returned a poor description of breaking pattern when rip currents were present on the nearshore, as already pointed out by Andriolo et al. [58]. Therefore, an automated algorithm to discard the low-quality images will be developed.

The preliminary test for video-derived breaking wave height is intended to be combined with the automated shoreline detection to build a video-based integrated system that will fully describe the nearshore hydrodynamics and morphology. Besides the breaking wave height and shoreline, the system is expected to provide nearshore bathymetry and hydrodynamics [27,33,59–62], wave runup [63–65] and intertidal topography [33,57].

5. Conclusions

This work evaluated the preliminary shoreline response to a sandy nourishment carried out in the wave-dominated Portuguese coast during summer 2019. In addition, this work constitutes the first high-frequency and high-resolution shoreline changes description at the study site, the Tarquínio-Paraiso beach.

Imagery collected by a coastal video monitoring station was used to draw up the nourishment calendar, and to quantify the emerged beach variation over six-months. Timex and Variance images were used to detect the shoreline, by manual and automated techniques, respectively.

The nourishment calendar showed that the phases of the works, namely tubing, injection and re-distribution of sand, started from the center of the beach and ended at the northern sector. For each of the six areas chosen to divide the beach, the three phases were usually completed in one day. Overall, the nourishment of the beach, measuring 390 m longshore, was finalized in ten days.

The nourishment works increased the cross-shore beach extension of 90 m on average. During high energy events in autumn, the shoreline retreated about 50 m. After six months, the emerged beach extent was about 30 m larger than it was prior to the nourishment, with a similar longshore configuration. The preliminary analysis of the beach response to the nourishment highlighted that the northern beach sector is the most vulnerable, with rapid beach extension decrease, as it is the downdrift side of the groin. Overall, the beach extent increased by the sand supply, preventing the usual flooding occurrences at Costa de Caparica, during high-energetic events, until the end of January.

The automated shoreline detection and video-derived breaking wave height were successfully tested and showed promising results, setting the ground for an automated video-based integrated system that will fully describe the nearshore hydrodynamics and morphology at the study site.

Author Contributions: Conceptualization, C.J.S., U.A. and J.C.F.; methodology, C.J.S., U.A.; software, C.J.S., U.A.; validation, C.J.S., U.A. and J.C.F.; formal analysis, C.J.S., U.A. and J.C.F.; investigation, C.J.S.; resources, C.J.S., U.A. and J.C.F.; data curation, C.J.S., U.A.; writing—Original draft preparation, C.J.S.; writing—Review and editing, C.J.S., U.A. and J.C.F.; visualization, C.J.S.; supervision, U.A., J.C.F.; project administration, U.A., J.C.F.; funding acquisition, U.A., J.C.F. All authors have read and agreed to the published version of the manuscript.

Funding: C.J.S. is supported by RISCO—Center for Environmental Risk Assessment and Management and Civil Protection (FCT NOVA—NOVA University of Lisbon); U.A. is supported by the project UAS4Litter (PTDC/EAM-REM/30324/2017) funded by the Portuguese Foundation for Science and Technology (FCT) and by UIDB/00308/2020. The authors also acknowledge the financial help of the FCT projects To-SEAlert (PTDC/EAM-OCE/31207/2017), BSAFE4SEA (PTDC/ECI-EGC/31090/2017), the MARE—Strategic program UID/MAR/04292/2019, and also to the ORLA—Observatory of Coastal Risks (FCT NOVA—Nova University of Lisbon).

Acknowledgments: The authors wish to thank Cláudio Macedo Duarte for the fundamental support in the video station installation and management, Ana Nobre Silva and Hugo Teixeira for the help during topographic surveys and image rectification, Rui Taborda for video station installation and project supervision. The authors would also like to acknowledge the Municipality of Almada and the Hotel "TRYP Lisboa Caparica Mar" for the logistical support in the video monitoring system installation.

Conflicts of Interest: The authors declare no conflict of interest.

References

1. Chiva, L.; Pagán, J.I.; López, I.; Tenza-Abril, A.J.; Aragonés, L.; Sánchez, I. The effects of sediment used in beach nourishment: Study case El Portet de Moraira beach. *Sci. Total Environ.* **2018**, *628–629*, 64–73. [CrossRef] [PubMed]
2. Karambas, T.V.; Samaras, A.G. Soft shore protection methods: The use of advanced numerical models in the evaluation of beach nourishment. *Ocean. Eng.* **2014**, *92*, 129–136. [CrossRef]
3. Luo, S.; Liu, Y.; Jin, R.; Zhang, J.; Wei, W. A guide to coastal management: Benefits and lessons learned of beach nourishment practices in China over the past two decades. *Ocean. Coast. Manag.* **2016**, *134*, 207–215. [CrossRef]
4. Karasu, S.; Work, P.A.; Uzlu, E.; Kankal, M.; Yüksek, Ö. Beach nourishment alternative assessment to constrain cross-shore and longshore sediment transport. *Appl. Ocean. Res.* **2016**, *59*, 459–471. [CrossRef]

5. Ludka, B.C.; Guza, R.T.; O'Reilly, W.C. Nourishment evolution and impacts at four southern California beaches: A sand volume analysis. *Coast. Eng.* **2018**, *136*, 96–105. [CrossRef]
6. Silva, S.F.; Martinho, M.; Capitão, R.; Reis, T.; Fortes, C.J.; Ferreira, J.C. An index-based method for coastal-flood risk assessment in low-lying areas (Costa de Caparica, Portugal). *Ocean. Coast. Manag.* **2017**, *144*, 90–104. [CrossRef]
7. Mahabot, M.M.; Jaud, M.; Pennober, G.; Le Dantec, N.; Troadec, R.; Suanez, S.; Delacourt, C. The basics for a permanent observatory of shoreline evolution in tropical environments; lessons from back-reef beaches in La Reunion Island. *C. R. Geosci.* **2017**, *349*, 330–340. [CrossRef]
8. Semeoshenkova, V.; Newton, A. Overview of erosion and beach quality issues in three Southern European countries: Portugal, Spain and Italy. *Ocean. Coast. Manag.* **2015**, *118*, 12–21. [CrossRef]
9. Andriolo, U. *Nearshore Hydrodynamics and Morphology Derived from Video Imagery*; Faculdade de Ciências da Universidade de Lisboa: Lisbon, Portugal, 2018.
10. Thurman, H.V.; Trujillo, A.P. *Essentials of Oceanography*, 6th ed.; Prentice Hall: Upper Saddle River, NJ, USA, 1999; ISBN 978-0-13-727348-5.
11. Boak, E.H.; Turner, I.L. Shoreline Definition and Detection: A Review. *J. Coast. Res.* **2005**, *214*, 688–703. [CrossRef]
12. Brignone, M.; Schiaffino, C.F.; Isla, F.I.; Ferrari, M. A system for beach video-monitoring: Beachkeeper plus. *Comput. Geosci.* **2012**, *49*, 53–61. [CrossRef]
13. Dewi, R.S.; Bijker, W. Dynamics of shoreline changes in the coastal region of Sayung, Indonesia. *Egypt. J. Remote Sens. Sp. Sci.* **2019**. [CrossRef]
14. García-Rubio, G.; Huntley, D.; Russell, P. Evaluating shoreline identification using optical satellite images. *Mar. Geol.* **2015**, *359*, 96–105. [CrossRef]
15. Hagenaars, G.; de Vries, S.; Luijendijk, A.P.; de Boer, W.P.; Reniers, A.J.H.M. On the accuracy of automated shoreline detection derived from satellite imagery: A case study of the sand motor mega-scale nourishment. *Coast. Eng.* **2018**, *133*, 113–125. [CrossRef]
16. Chen, W.-W.; Chang, H.-K. Estimation of shoreline position and change from satellite images considering tidal variation. *Estuar. Coast. Shelf Sci.* **2009**, *84*, 54–60. [CrossRef]
17. Vos, K.; Splinter, K.D.; Harley, M.D.; Simmons, J.A.; Turner, I.L. CoastSat: A Google Earth Engine-enabled Python toolkit to extract shorelines from publicly available satellite imagery. *Environ. Model. Softw.* **2019**, *122*, 104528. [CrossRef]
18. Holthuijsen, L.H. *Waves in Oceanic and Coastal Waters*; Cambridge University Press: Cambridge, UK, 2007; ISBN 978051126.
19. Vos, K.; Harley, M.D.; Splinter, K.D.; Simmons, J.A.; Turner, I.L. Sub-annual to multi-decadal shoreline variability from publicly available satellite imagery. *Coast. Eng.* **2019**, *150*, 160–174. [CrossRef]
20. Sánchez-García, E.; Balaguer-Beser, Á.; Almonacid-Caballer, J.; Pardo-Pascual, J.E. A new adaptive image interpolation method to define the shoreline at sub-pixel level. *Remote Sens.* **2019**, *11*, 1880. [CrossRef]
21. Ponte Lira, C.; Silva, A.N.; Taborda, R.; De Andrade, C.F. Coastline evolution of Portuguese low-lying sandy coast in the last 50 years: An integrated approach. *Earth Syst. Sci. Data* **2016**, *8*, 265–278. [CrossRef]
22. Splinter, K.; Harley, M.; Turner, I. Remote Sensing Is Changing Our View of the Coast: Insights from 40 Years of Monitoring at Narrabeen-Collaroy, Australia. *Remote Sens.* **2018**, *10*, 1744. [CrossRef]
23. Andriolo, U.; Sánchez-García, E.; Taborda, R. Operational use of surfcam online streaming images for coastal morphodynamic studies. *Remote Sens.* **2019**. [CrossRef]
24. Holman, R.A.; Stanley, J. The history and technical capabilities of Argus. *Coast. Eng.* **2007**, *54*, 477–491. [CrossRef]
25. Angnuureng, D.B. *Shoreline Response to multi-Scale Oceanic Forcing from Video Imagery*; Université de Bordeaux: Bordeaux, France, 2016.
26. Archetti, R.; Vacchi, M.; Bertoncini, L.; Conserva, R.; Michela, S.; Sigismondi, D.; Parlagreco, L. Coastal monitoring through video systems: best practices and architectural design of a new video monitoring network at Marina di Massa (Tuscany). *Coast. Eros. Monit.—A Netw. Reg. Obs. Results from ResMar Proj.* **2013**, *15*, 157–167.
27. Andriolo, U. Nearshore Wave Transformation Domains from Video Imagery. *J. Mar. Sci. Eng.* **2019**, *7*, 186. [CrossRef]

28. Guedes, R.M.C.; Calliari, L.J.; Holland, K.T.; Plant, N.G.; Pereira, P.S.; Alves, F.N.A. Short-term sandbar variability based on video imagery: Comparison between Time-Average and Time-Variance techniques. *Mar. Geol.* **2011**, *289*, 122–134. [CrossRef]
29. Vousdoukas, M.I.; Almeida, L.P.M.; Ferreira, Ó. Beach erosion and recovery during consecutive storms at a steep-sloping, meso-tidal beach. *Earth Surf. Process. Landf.* **2012**, *37*, 583–593. [CrossRef]
30. Valentini, N.; Saponieri, A.; Molfetta, M.G.; Damiani, L. New algorithms for shoreline monitoring from coastal video systems. *Earth Sci. Inform.* **2017**, *10*, 495–506. [CrossRef]
31. Bracs, M.A.; Turner, I.L.; Splinter, K.D.; Short, A.D.; Lane, C.; Davidson, M.A.; Goodwin, I.D.; Pritchard, T.; Cameron, D. Evaluation of Opportunistic Shoreline Monitoring Capability Utilizing Existing "Surfcam" Infrastructure. *J. Coast. Res.* **2016**, *319*, 542–554. [CrossRef]
32. Uunk, L.; Wijnberg, K.M.; Morelissen, R. Automated mapping of the intertidal beach bathymetry from video images. *Coast. Eng.* **2010**, *57*, 461–469. [CrossRef]
33. Vousdoukas, M.I.; Ferreira, P.M.; Almeida, L.P.; Dodet, G.; Psaros, F.; Andriolo, U.; Taborda, R.; Silva, A.N.; Ruano, A.; Ferreira, Ó.M. Performance of intertidal topography video monitoring of a meso-tidal reflective beach in South Portugal. *Ocean. Dyn.* **2011**, *61*, 1521–1540. [CrossRef]
34. Valentini, N.; Saponieri, A.; Damiani, L. A new video monitoring system in support of Coastal Zone Management at Apulia Region, Italy. *Ocean. Coast. Manag.* **2017**, *142*, 122–135. [CrossRef]
35. Plant, N.G.; Holman, R. A Intertidal beach profile estimation using video images. *Mar. Geol.* **1997**, *140*, 1–24. [CrossRef]
36. Aarninkhof, S.G.J.; Turner, I.L.; Dronkers, T.D.T.; Caljouw, M.; Nipius, L. A video-based technique for mapping intertidal beach bathymetry. *Coast. Eng.* **2003**, *49*, 275–289. [CrossRef]
37. Simarro, G.; Bryan, K.R.; Guedes, R.M.C.; Sancho, A.; Guillen, J.; Coco, G. On the use of variance images for runup and shoreline detection. *Coast. Eng.* **2015**, *99*, 136–147. [CrossRef]
38. Splinter, K.D.; Strauss, D.R.; Tomlinson, R.B. Assessment of post-storm recovery of beaches using video imaging techniques: A case study at Gold Coast, Australia. *IEEE Trans. Geosci. Remote Sens.* **2011**, *49*, 4704–4716. [CrossRef]
39. Archetti, R.; Zanuttigh, B. Integrated monitoring of the hydro-morphodynamics of a beach protected by low crested detached breakwaters. *Coast. Eng.* **2010**, *57*, 879–891. [CrossRef]
40. Osorio, A.F.; Medina, R.; Gonzalez, M. An algorithm for the measurement of shoreline and intertidal beach profiles using video imagery: PSDM. *Comput. Geosci.* **2012**, *46*, 196–207. [CrossRef]
41. Brodie, K.L.; Bruder, B.L.; Slocum, R.K.; Spore, N.J. Simultaneous Mapping of Coastal Topography and Bathymetry from a Lightweight Multicamera UAS. *IEEE Trans. Geosci. Remote Sens.* **2019**, *57*, 6844–6864. [CrossRef]
42. Elko, N.A.; Holman, R.A.; Gelfenbaum, G. Quantifying the Rapid Evolution of a Nourishment Project with Video Imagery. *J. Coast. Res.* **2005**, *214*, 633–645. [CrossRef]
43. Harley, M.D.; Andriolo, U.; Armaroli, C.; Ciavola, P. Shoreline rotation and response to nourishment of a gravel embayed beach using a low-cost video monitoring technique: San Michele-Sassi Neri, Central Italy. *J. Coast. Conserv.* **2014**, *18*, 551–565. [CrossRef]
44. Ojeda, E.; Guillén, J. Monitoring beach nourishment based on detailed observations with video measurements. *J. Coast. Res.* **2006**, *7*, 100–106.
45. Brignone, M.; Corradi, N.; Ferrari, M.; Schiaffino, C.F. Evaluation of a nourishment programme with a webcam: The case of Levanto (La Spezia, Italy). *Chem. Ecol.* **2008**, *24*, 207–214. [CrossRef]
46. Ambiente, A.P. Do Alimentação Artificial de Praias na Costa de Caparica. Available online: https://apambiente.pt/ajaxpages/destaque.php?id=1287 (accessed on 18 May 2020).
47. Marinho, B.; Coelho, C.; Hanson, H.; Tussupova, K. Coastal management in Portugal: Practices for reflection and learning. *Ocean. Coast. Manag.* **2019**, *181*, 104874. [CrossRef]
48. Silva, A.N.; Taborda, R.; Andrade, C.; Ribeiro, M. The future of insular beaches: Insights from a past-to-future sediment budget approach. *Sci. Total Environ.* **2019**, *676*, 692–705. [CrossRef] [PubMed]
49. Veloso-Gomes, F.; Costa, J.; Rodrigues, A.; Taveira-Pinto, F.; Pais-Barbosa, J.; Neves, L. Costa da Caparica Artificial Sand Nourishment and Coastal Dynamics. *J. Coast. Res.* **2009**, *56*, 678–682.
50. Dodet, G.; Bertin, X.; Taborda, R. Wave climate variability in the North-East Atlantic Ocean over the last six decades. *Ocean. Model.* **2010**, *31*, 120–131. [CrossRef]

51. Bouguet, J.-Y. Camera Calibration Toolbox for Matlab. Available online: http://www.vision.caltech.edu/bouguetj/calib_doc/ (accessed on 18 May 2020).
52. Taborda, R.; Silva, A. COSMOS: A lightweight coastal video monitoring system. *Comput. Geosci.* **2012**, *49*, 248–255. [CrossRef]
53. Sánchez-García, E.; Balaguer-Beser, A.; Pardo-Pascual, J.E. C-Pro: A coastal projector monitoring system using terrestrial photogrammetry with a geometric horizon constraint. *ISPRS J. Photogramm Remote Sens.* **2017**, *128*, 255–273. [CrossRef]
54. Chang, Y.S.; Jin, J.Y.; Jeong, W.M.; Kim, C.H.; Do, J.D. Video Monitoring of Shoreline Positions in Hujeong Beach, Korea. *Appl. Sci.* **2019**, *9*, 4984. [CrossRef]
55. Emami, A.; Bryan, K.R.; Lange, W.P. de Spatial Patterns in Groundwater Seepage and Surf Zone Morphology: Muriwai Beach, New Zealand. *J. Coast. Res.* **2019**, *35*, 186. [CrossRef]
56. Pearre, N.S.; Puleo, J.A. Quantifying Seasonal Shoreline Variability at Rehoboth Beach, Delaware, Using Automated Imaging Techniques. *J. Coast. Res.* **2009**, *254*, 900–914. [CrossRef]
57. Andriolo, U.; Almeida, L.P.; Almar, R. Coupling terrestrial LiDAR and video imagery to perform 3D intertidal beach topography. *Coast. Eng.* **2018**, *140*, 232–239. [CrossRef]
58. Andriolo, U.; Mendes, D.; Taborda, R. Breaking Wave Height Estimation from Timex Images: Two Methods for Coastal Video Monitoring Systems. *Remote Sens.* **2020**, *12*, 204. [CrossRef]
59. Abessolo Ondoa, G.; Almar, R.; Kestenare, E.; Bahini, A.; Houngue, G.-H.; Jouanno, J.; Du Penhoat, Y.; Castelle, B.; Melet, A.; Meyssignac, B.; et al. Potential of Video Cameras in Assessing Event and Seasonal Coastline Behaviour: Grand Popo, Benin (Gulf of Guinea). *J. Coast. Res.* **2016**, *75*, 442–446. [CrossRef]
60. Almar, R.; Cienfuegos, R.; Catalán, P.A.; Birrien, F.; Castelle, B.; Michallet, H. Nearshore bathymetric inversion from video using a fully non-linear Boussinesq wave model. *J. Coast. Res.* **2011**, *64*, 3–7.
61. Thuan, D.H.; Almar, R.; Marchesiello, P.; Viet, N.T. Video Sensing of Nearshore Bathymetry Evolution with Error Estimate. *J. Mar. Sci. Eng.* **2019**, *7*, 233. [CrossRef]
62. Abessolo Ondoa, G.; Almar, R.; Castelle, B.; Testut, L.; Léger, F.; Sohou, Z.; Bonou, F.; Bergsma, E.W.J.; Meyssignac, B.; Larson, M. Sea level at the coast from video-sensed waves: Comparison to tidal gauges and satellite altimetry. *J. Atmos. Ocean. Technol.* **2019**, *36*, 1591–1603. [CrossRef]
63. Guedes, R.M.C.; Bryan, K.R.; Coco, G.; Holman, R.A. The effects of tides on swash statistics on an intermediate beach. *J. Geophys. Res. Ocean.* **2011**, *116*, 1–13. [CrossRef]
64. Almar, R.; Blenkinsopp, C.; Almeida, L.P.; Cienfuegos, R.; Catalán, P.A. Wave runup video motion detection using the Radon Transform. *Coast. Eng.* **2017**, *130*, 46–51. [CrossRef]
65. Senechal, N.; Coco, G.; Bryan, K.R.; Holman, R.A. Wave runup during extreme storm conditions. *J. Geophys. Res. Ocean.* **2011**, *116*. [CrossRef]